Thermal conductance of pillar-based phononic crystals at sub-Kelvin temperatures

Master's thesis, 16.11.2020

Author:

Tatu Korkiamäki

Supervisor:

Ilari Maasilta

UNIVERSITY OF JYVÄSKYLÄ
DEPARTMENT OF PHYSICS

Abstract

Korkiamäki, Tatu

Thermal conductance of pillar-based phononic crystals at sub-Kelvin temperatures
Masters thesis
Department of Physics, University of Jyväskylä, 2020, 99 pages.

A phononic crystal (PnC) is an artificial periodic structure in one, two or three dimensions that affects the propagation of phonons, the quanta of elastic waves. As heat is mostly carried by phonons in insulators and semiconductors, PnC can be utilised in controlling thermal transport in such materials. The mechanisms how PnCs can work can be generally divided into two categories: one where incoherent, diffusive particle-like scattering dominates, and another where coherent wave-like scattering is operational. Compared to hole-based PnCs, much less studied 2D crystals in thermal conductance manipulation are the pillar-based PnCs, where the lattice is formed by a periodic array of pillars on a thin membrane. For such PnCs, the phonon spectrum can also include localised resonances which cannot carry heat.

In this thesis we have fabricated and measured the thermal conductance of two pillar-based PnC with a different lattice constant, where aluminium pillars with a height of 300 nm, a 0.65 filling factor and lattice constants of 5 μm and 1 μm were deposited on a 300 nm thick silicon nitride film. The measurements were conducted at sub-Kelvin temperatures with a superconducting junction-based heater-thermometer setup fabricated onto the sample. Low temperatures were achieved via a ^{3}He/^{4}He dilution refrigerator. The results showed up to an 85 % reduction in thermal conductance compared to an unaltered film. Initially, it appears that the mechanism responsible for the reduction was incoherent scattering. Possible causes for the breakdown of the coherence include the pillar surface roughness, the pillar-film-interface, or grain boundaries within the pillars.

Keywords: phononic crystal, pillar-based, thermal conductance, coherence

Tiivistelmä

Korkiamäki, Tatu
Pilaripohjaisten fononikiteiden lämmönjohtavuus alle Kelvinin lämpötilassa
Pro gradu
Fysiikan laitos, Jyväskylän yliopisto, 2020, 99 sivua

Fononikide on keinotekoinen periodinen rakenne yhdessä, kahdessa tai kolmessa ulottuvuudessa, joka vaikuttaa fononien eli elastisten aaltojen kvanttien etenemiseen. Koska lämmön johtuminen eristeissä ja puolijohteissa tapahtuu pääasiassa fononien välityksellä, voidaan fononikiteillä vaikuttaa lämmön kulkeutumiseen kyseisissä materiaaleissa. Fononikiteiden toimintamekanismit voidaan karkeasti jakaa kahteen eri kategoriaan: epäkoherenttiin, jossa hiukkasmainen diffusiivinen sironta hallitsee, ja koherenttiin, jossa fononit etenevät aaltomaisesti. Verrattuna reikärakenteisiin perustuviin kiteisiin, lämmönjohtumiseen vaikuttavien fononikiteiden joukossa huomattavasti vähemmän tutkittuja 2D-kiteitä ovat niin kutsutut pilaripohjaiset fononikiteet, joissa hila muodostuu periodisesti järjestyneistä pilareista ohuella kalvolla. Näiden fononikiteiden spektri voi sisältää niin kutsuttuja lokaaleja resonansseja, jotka estävät lämmön kulkeutumisen.

Tässä pro gradu -tutkielmassa valmistettiin kaksi pilaripohjaista fononikidettä eri hilavakiolla, joiden lämmönjohtavuudet mitattiin. Pilareiden materiaali oli alumiini, ja niiden korkeus oli 300 nm, täyttösuhde oli 0.65, hilavakiot olivat 5 μm ja 1 μm, ja ne olivat 300 nm paksun piinitridikalvon pinnalla. Mittaukset suoritettiin suprajohtaviin liitoksiin perustuvalla lämmitin-lämpömittari-laitteella, joka valmistettiin näytteelle. Mittaukset tehtiin alle Kelvinin lämpötilassa, joka saavutettiin ^{3}He/^{4}He-laimennusjäähdyttimellä. Tuloksina saatiin 85 %:n lämmönjohtavuuden aleneminen verrattuna puhtaaseen kalvoon, joka kuitenkin vaikuttaisi olevan peräisin epäkoherentista sironnasta. Mahdollisia syitä koherenssin katoamiselle ovat pilareiden pinnan epätasaisuus, pilareiden ja kalvon välinen rajapinta sekä pilareiden sisäiset raerajat.

Avainsanat: fononikide, pilaripohjainen, lämmönjohtavuus, koherenssi

Preface

Mitata voi keinoin valmistetun mittarin
Mittarikaan ei voi näyttää sisintä mysteerin
- Rättö ja Lehtisalo, Valonnopeus (2003)

To begin with, I would like thank Prof. Ilari Maasilta for allowing me to work with this fascinating project. It has been truly a great experience working with the group for the past 1.5 years, since I started as a summer trainee in 2019.

Of the practical work involved with this thesis, I would like to especially thank Dr. Tuomas Puurtinen for providing the simulations involved in this work, and for discussions involving the simulations and theory. I am also extremely thankful for staff scientist Dr. Kimmo Kinnunen and laboratory engineer Mr. Tarmo Suppula for ensuring that everything in the lab worked properly. I would also like to thank the rest of the research group members, and especially Mr. Teemu Loippo for instructing me with fabrication related issues, Mr. Ilmo Räisänen whom I did the low temperature measurements with, Mr. Samuli Heiskanen, Mr. Geng Zhuoran and Mr. Ari Helenius for assisting with the cooldowns, and also Mr. Aki Ruhtinas for insightful discussions and peer support.

Of course, I would also like to thank my girlfriend and family for support during this thesis project, and support from my friends is also greatly appreciated.

Jyväskylä, November 2020

Tatu Korkiamäki

Contents

1 Introduction

A phonon can be understood as the quantum of an elastic wave. The name phonon implies an analogy with photon, the quantum of electromagnetic waves. The field of phononics covers the alteration of elastic wave propagation from sound and vibrations in earths crust, or vibrations in the order of Hz, to thermal vibrations which can extend to the order of THz [1]. Since the existence of phononic band gaps in a periodic elastic medium was predicted in 1993 [2], there has been an increasing interest in phononics and its potential applications.

Materials with an artificially created periodicity in one, two or three dimensions which alter the phonon spectrum by creating so-called band gaps are called phononic crystals (PnC). A perhaps more well known and well studied analogue to phononic crystals are photonic crystals, which are artificial periodic structures created to control the propagation of photons [3]. A band gap created by the periodicity prevents certain frequencies of elastic waves from propagating within the material [4]. The frequencies which are affected by the phononic crystal are inversely proportional to the periodicity of the PnC, so with developing fabrication methods manipulation of phonons of increasingly high frequencies has been realised.

The main goals in phononics dealing with the thermal frequency range include increasing the effectiveness of semiconducting devices by reducing thermal conductivity, creating more well isolated systems for more sensitive detectors by increasing thermal insulation and reducing thermal noise [5, 6]. PnCs can perhaps be utilised in quantum computing either in isolation or computation [7–9]. It is also possible to guide, filter and multiplex acoustic waves [10] and even to achieve a wave-like control of heat via various waveguide systems [5]. Phononic crystals can also function as a radiation detector by themselves [11].

Controlling thermal transport with PnCs can be divided into two categories: coherent and incoherent effects. Incoherent effects generally dominate at high temperatures where diffusive scattering is the main contributor to thermal resistance, whereas coherent effects begin to become significant at low temperatures, and are dominant

in the sub-Kelvin region. In the coherent regime phonons act like waves, and can be controlled as such by Bragg-like interference [1, 12].

In 1D coherent effects and the conditions to achieve them are well documented [13–17], but until fairly recently results of coherent effects in higher dimensions have remained absent or inconclusive [18–20]. In recent years, significant numerical and even experimental results have been obtained of coherent thermal transport control at low temperatures with 2D PnCs [1, 10, 18, 19, 21].

These results have mainly focused on hole-based PnC structures on thin films. However, there exists another type of 2D-PnCs called pillar-based phononic crystal, where the geometry can be described as pillars on a periodic array on top of a film or a plate, and the band gaps are introduced to the spectrum by so-called local resonances [4, 10]. The first results for a locally resonant PnC were presented in 2000 [22]. Pillar-based PnCs have been rather extensively studied in the sonic range (frequencies near audible sound frequencies) [4, 10], but little research has been conducted on pillar-based PnCs in the thermal frequencies, and even less attention has been given to the low temperature regime [23].

An extensive study has been conducted in our research group on phononics at low temperatures, including studies on thermal conductance reduction with hole-based PnCs [18, 21, 24]. This existing knowledge is extended in this thesis, where pillar-based PnCs with aluminium pillars on a 300 nm silicon nitride (SiN) film are fabricated, and the thermal conductance is measured with well-established methods. The measured thermal conductance of the PnC is compared to the thermal conductance of an unmodified SiN film and to numerical simulations to discover whether numerical results in the ballistic regime are in agreement with experiments for these structures.

These pillar-based PnCs can be utilised in much the same way as hole-based PnC in detector applications. An application where pillar-based PnCs could actually be superior to their hole-based counterpart is in semiconducting thermoelectric materials, where PnCs can notably increase their efficiency [5]. This efficiency is described by the thermoelectric figure of merit $ZT \propto \sigma/\kappa$, where σ is the electrical and κ is the thermal conductance. The improvement stems from the fact that with hole-based PnCs κ is significantly reduced, while σ is only slightly lowered in the best case scenario. In pillar-based structures however the ZT can be even better, as the

film itself is not impaired in any way, leaving the electrical conductivity completely unaltered [25, 26]. The creation of holes also inevitably creates some roughness in the hole surfaces which introduces nonidealities, whereas in the case of pillar-based PnCs the film again remains unaltered.

2 Theoretical background

2.1 Thermal conduction at low temperatures

2.1.1 Thermal transport in insulators

Phonons are collective excitations of elastic vibrations in a lattice. They are responsible for sound transport in solids, and heat conduction in insulators and semiconductors. This is in contrast to metals, where electrons are responsible for a significant portion of heat conduction.

Phonons behave like bosons, and thus obey Bose-Einstein statistics with an occupation number of the form

$$n_B = \frac{1}{e^{\beta\hbar\omega} - 1}, \tag{1}$$

where $\hbar$ is the reduced Planck constant, ω is the phonon frequency and $\beta = (k_B T)^{-1}$, where k_B is the Boltzmann constant and T is temperature [27].

It is convenient to consider the propagation of phonons in the k-space, a three-dimensional Cartesian space with axes k_x, k_y and k_z. Each allowed wave vector $\mathbf{k}$ occupies a k-space volume $(2\pi)^3/V$, giving a k-space density of states [28]

$$\frac{V}{(2\pi)^3}. \tag{2}$$

For periodic systems an essential tool is the reciprocal lattice. It is defined by the vectors $\mathbf{K}$ that give out plane wave solutions with the periodicity of a given Bravais lattice of points $\mathbf{R}$ [28]

$$e^{i\mathbf{K}\cdot(\mathbf{r}+\mathbf{R})} = e^{i\mathbf{K}\cdot\mathbf{r}}, \tag{3}$$

or

$$e^{i\mathbf{K}\cdot\mathbf{R}} = 1. \tag{4}$$

The first Brillouin zone is a primitive cell in the reciprocal lattice defined as the unit cell created by enclosing a lattice point with planes normal to a line between two

lattice points, the planes intersecting the lines at the middle point of each line. The reciprocal lattice primitive vectors can be defined by the Bravais lattice primitive vectors $\mathbf{a}_1$, $\mathbf{a}_2$, $\mathbf{a}_3$ as

$$\mathbf{b}_1 = 2\pi \frac{\mathbf{a}_2 \times \mathbf{a}_3}{\mathbf{a}_1 \cdot \mathbf{a}_1(\mathbf{a}_2 \times \mathbf{a}_3)},\ \mathbf{b}_2 = 2\pi \frac{\mathbf{a}_3 \times \mathbf{a}_1}{\mathbf{a}_1 \cdot \mathbf{a}_1(\mathbf{a}_2 \times \mathbf{a}_3)},\ \mathbf{b}_3 = 2\pi \frac{\mathbf{a}_1 \times \mathbf{a}_2}{\mathbf{a}_1 \cdot \mathbf{a}_1(\mathbf{a}_2 \times \mathbf{a}_3)}. \quad (5)$$

With the primitive vectors, the reciprocal lattice vector $\mathbf{K}$ can be written as

$$\mathbf{K} = v_1\mathbf{b}_1 + v_2\mathbf{b}_2 + v_3\mathbf{b}_3, \quad (6)$$

where v_n are integers. We can also write any arbitrary $\mathbf{k}$ in the reciprocal space as a linear combination of the reciprocal lattice primitive vectors:

$$\mathbf{k} = k_1\mathbf{b}_1 + k_2\mathbf{b}_2 + k_3\mathbf{b}_3. \quad (7)$$

The atomic displacements can be expressed as a travelling wave with the displacements of individual atoms, at vector $\mathbf{R}_i$ as functions $\mathbf{k}$ [29]:

$$u_i(\mathbf{k},s,\mathbf{R},t) = \sum_{\mathbf{k},s} \mathbf{u}(\mathbf{k},s)e^{i(\mathbf{k}\cdot\mathbf{R}_i - \omega t)}, \quad (8)$$

where s is the mode index. Any elastic wave in a periodic lattice can be described with wave vectors in the first Brillouin zone. [28, 29]

The distinction between high and low temperatures is typically done by considering the Debye model of lattice waves. The Debye model assumes only three isotropic acoustic modes of the vibrational spectrum with linear dispersion relations

$$\omega = ck, \quad (9)$$

where c are the average speeds of each acoustic mode, or the speeds of sound, defined as [30]

$$\frac{3}{c^3} = \left(\frac{1}{c_l^3} + \frac{1}{c_{t1}^3} + \frac{1}{c_{t2}^3}\right) \quad (10)$$

for the three phonon modes, one longitudinal c_l and two transverse c_{t1} and c_{t2}.

Here the Brillouin zone is replaced by a sphere of radius k_D, which contains N allowed wave vectors, where N is the number of atoms. k_D is thus defined by the

k-space density of states (equation (2))

$$\frac{N}{V} = \frac{k_D^3}{6\pi^2}. \tag{11}$$

The lattice specific heat of the Debye model is

$$C = \frac{\partial Q}{\partial T} = \frac{3\hbar c}{2\pi^2}\frac{\partial}{\partial T}\int_0^{k_D} \frac{dkk^3}{(e^{\beta\hbar\omega}-1)^2}. \tag{12}$$

By defining the Debye frequency

$$\omega_D = ck_D \tag{13}$$

and the Debye temperature

$$\Theta_D = k_B\omega_D \tag{14}$$

in terms of k_D, and making the substitution $\beta\hbar\omega = x$, one can write equation (12) in the following form:

$$C = 9nk_B\left(\frac{T}{\Theta_D}\right)^3 \int_0^{\Theta_D/T} \frac{x^4e^x dx}{(e^x-1)^2}. \tag{15}$$

The physical significance of Θ_D is that is gives a temperature limit above which all modes are exited, and below which modes begin to "freeze out". This is apparent as we look at equation (15): When $T \ll \Theta_D$, the integral part can be solved to obtain a simple T^3 dependence. This makes Θ_D an useful tool in defining the difference between high and low temperatures for a solid. [28]

Equation (15) is valid for a 3D phonon gas. The equation for 2D heat capacity can be derived from equation (12) in the low temperature limit by making the same change of variables as above, resulting in [31]

$$C_{2D} = \frac{3\zeta(3)}{\pi}\frac{k_B^3}{\hbar^2}\left(\frac{1}{c_l^2}+\frac{2}{c_t^2}\right)T^2, \tag{16}$$

where ζ is the Riemann zeta function.

Another useful tool obtained from the Debye model is the dominant thermal phonon

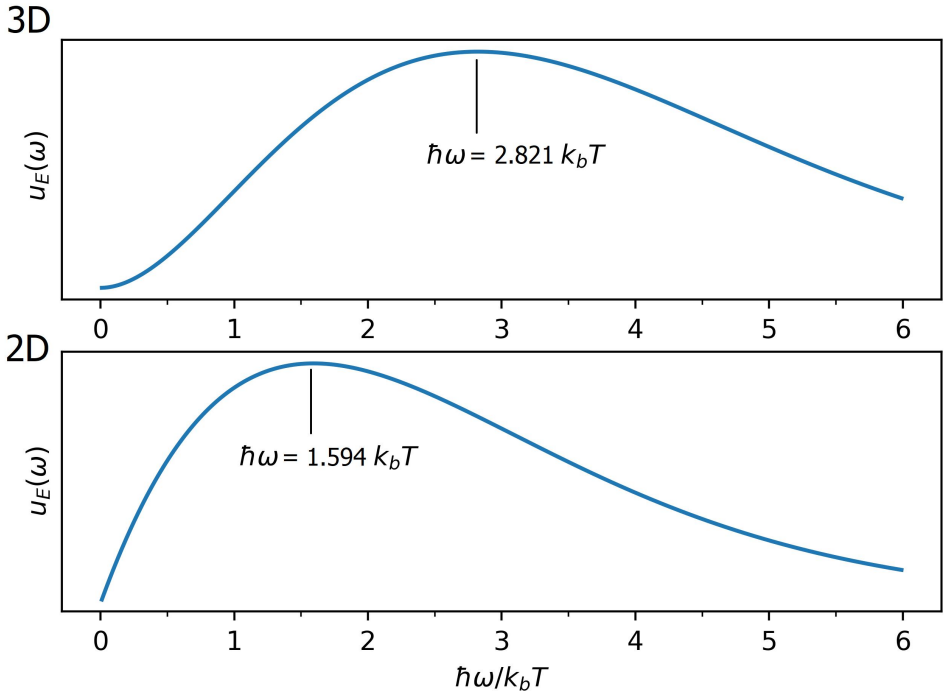

Figure 1. Phonon spectral energy density for 3D and 2D phonon gases.

wavelength. The spectral phonon energy density from the Debye model is [30]

$$u_E(\omega) = \frac{\hbar\omega}{e^{\beta\hbar\omega} - 1} D(\omega), \tag{17}$$

where $D(\omega)$ is the Debye density of states, given by [30]

$$D_{3D}(\omega) = \frac{3\omega^2}{2\pi^2 c^3} \tag{18}$$

for a 3D phonon gas, and by [32]

$$D_{2D}(\omega) = \frac{\omega}{2\pi c^2} \tag{19}$$

for a 2D gas. A is the area. Thus, the spectral phonon energy densities in 3D and 2D are

$$u_{E\,3D}(\omega) = \frac{3\hbar}{2\pi^2 c^3} \frac{\omega^3}{e^{\beta\hbar\omega} - 1}, \tag{20}$$

and

$$u_{E\,2D}(\omega) = \frac{\hbar}{2\pi c^2} \frac{\omega^2}{e^{\beta\hbar\omega} - 1}, \tag{21}$$

respectively. These are plotted in Figure 1. Knowing the peak value constant B of the spectrum, 2.821 for a 3D and 1.594 for a 2D gas [18, 30], one can easily calculate the dominant phonon frequency

$$\omega_{dom} = \frac{Bk_BT}{\hbar}, \tag{22}$$

and the dominant wavelength

$$\lambda_{dom} = \frac{2\pi c}{\omega_{dom}} \tag{23}$$

for a given temperature.

At high temperatures, when $T > \Theta_D$, most of the thermal resistance is attributed to inelastic phonon-phonon-phonon scattering. When considering phonons, it is important to note that a plane wave does not transport a net momentum, and $\hbar\mathbf{k}$ is referred to as the crystal momentum. A consequence of this is that crystal momentum need not be conserved in phonon-phonon collisions, as opposed to say collisions in an ideal gas.

A simple three phonon interaction, where two phonons coalesce into one, can be described by the equation

$$\mathbf{k}_1 + \mathbf{k}_2 = \mathbf{k}_3 + \mathbf{G}, \tag{24}$$

where $\mathbf{k}_1$ and $\mathbf{k}_2$ are the incoming phonons, $\mathbf{k}_3$ is the resulting phonon and $\mathbf{G}$ is a reciprocal lattice vector. Processes when $\mathbf{G} = 0$ are called normal processes, and these collisions conserve crystal momentum and do not contribute to thermal resistance. When $\mathbf{G} \neq 0$ the process is called an Umklapp process. In sufficiently high temperatures the sum vector $\mathbf{k}_3$ may be large enough to reach to an adjacent Brillouin zone. As only the wave vectors in the first Brillouin zone are significant, the k-vector is "returned" to the first zone by $\mathbf{G}$. This results in a loss of (crystal) momentum and creates a heat resistance. [27]

A general kinetic formula for the thermal conductivity in three dimensions is

$$\kappa = \frac{1}{3}Cv\Lambda, \tag{25}$$

where v is the appropriately averaged phonon velocity and Λ is the mean free path of phonons. At high temperatures, or when Umklapp scattering is the dominant mechanism of heat resistance, the mean free path, and thus the thermal conductivity,

are inversely proportional to temperature [27]:

$$\Lambda \propto \frac{1}{T}, \quad \kappa \propto \frac{1}{T}, \quad \text{when } T > \Theta_D. \tag{26}$$

When $T < \Theta_D$ Umklapp processes quickly freeze out, as for long phonon wavelengths they are not possible [27]. In the absence of inelastic scattering the main source of heat resistance is boundary scattering, or scattering from lattice imperfections and specimen surfaces. This can allow Λ to drastically increase. In a length scale $< \Lambda$, phonon propagation is referred to as ballistic. At very low temperatures, where phonon wavelengths can be in the μm scale [24], this ballistic regime can be macroscopic. Ballistic transport has been reported to be dominant in silicon nitride at 0.1 mK in length scales of $0.1 - 1$ mm [18, 33].

Another essential concept to define is coherence. A collection of waves is coherent if they have a constant phase difference and an identical frequency. Coherence also requires specular scattering from interfaces preserving the phase, as diffusive scattering destroys the coherence [12]. In a simplified manner it can be said that incoherent phonons act like particles, whereas coherent phonons propagate as waves. Thermal phonons as a whole are incoherent, as they are created by a random motion in a lattice [12]. Thus, in the context of thermal transport, when talking about coherence it is considered spectrally, i.e. separately for each frequency. It is clear, that for phonons to behave coherently they are also required to propagate ballistically.

The proportion of specular surface scattering is approximated by the following model by Ziman [27], which has been corrected according to a revision by Maznev [34]:

$$P(\lambda) = \exp\left(-\frac{16\pi^2\eta^2}{\lambda^2}\right), \tag{27}$$

where η is the root mean square roughness of the surface and λ is the phonon wavelength. This can be interpreted so that for a given roughness coherent phonon propagation becomes significant only below a certain temperature, where the dominant phonon wavelength is longer than η.

Using (22) and (23), at 0.1 K for SiN the $\lambda_{dom} \approx 1700$ nm, if 5800 m/s [18] is used for the speed of sound. The RMS surface roughness of a SiN film is < 1 nm in the commercial films used by our group [35]. From equation (27), the proportion of

specular scattering with these parameters is $P(\lambda) \approx 0.99994$, decreasing to 0.994 at 1 K. As 1 K is essentially the upper limit for the range of the measurements and the films studied are 300 × 300 µm, within the range of ballistic phonon propagation in SiN, it can be assumed that coherent effects are dominant in the case of a pristine membrane.

2.1.2 Elastic waves in a suspended membrane

As has now been established, phonons propagate ballistically at a given temperature and length scale in a material with smooth enough surfaces. In these circumstances, thermal transport in a membrane can be understood simply as propagation of elastic waves in a plate. The results for elastic wave propagating in a plate, an object that a suspended thin film can be considered as, were first presented by Rayleigh and Lamb in 1889 [36].

We consider a semi-infinite plate with a thickness of $2d$ in the y-direction. An SH-wave is a shear wave which is horizontally polarised, meaning displacements only in a single direction are allowed. For a plate with traction free boundaries in the $y = \pm d$ direction, wave displacements for an SH-wave travelling in the x-direction are in the z-direction, and are of the form

$$u_z = [A_1 \sin(\beta y) + A_2 \cos(\beta y)]e^{i\varphi}, \tag{28}$$

where A_1 and A_2 are amplitudes for the waves, and $\varphi = \xi x - \omega t$ is the phase. β is defined as

$$\beta = \frac{\omega^2}{c_t^2} - \xi^2, \tag{29}$$

where ξ is a wavenumber.

From equation (28) one can solve the frequency equation

$$\cos(\beta d)\sin(\beta d) = 0, \tag{30}$$

which is satisfied by

$$\beta d = \frac{n\pi}{2}, \quad \text{where } n = 0, 1, 2, \ldots . \tag{31}$$

The wave modes with displacements in the remaining two directions are called the symmetric and antisymmetric Lamb modes. For a plate with similar boundary conditions, symmetric wave displacements travelling in the x-direction are of the form [36]

$$u_x = i[B\xi\cos(\alpha y) + C\beta\cos(\beta y)]e^{i\varphi}, \tag{32}$$

$$u_y = -[B\alpha\sin(\alpha y) - C\xi\sin(\beta y)]e^{i\varphi}. \tag{33}$$

Here α is a similar coefficient to β, but for longitudinal waves:

$$\alpha^2 = \frac{\omega^2}{c_l^2} - \xi^2. \tag{34}$$

The corresponding antisymmetric displacements are

$$u_x = i[A\xi\sin(\alpha y) - D\beta\sin(\beta y)]e^{i\varphi}, \tag{35}$$

$$u_y = [A\alpha\cos(\alpha y) + D\xi\cos(\beta y)]e^{i\varphi}, \tag{36}$$

and A, B, C, D are amplitudes for the waves. From equations (32) and (33), and from the boundary conditions one can derive the symmetric Rayleigh-Lamb frequency equation

$$\frac{\tan(\beta d)}{\tan(\alpha d)} = -\frac{4\alpha\beta\xi^2}{(\xi^2 - \beta^2)^2}. \tag{37}$$

Similarly, the antisymmetric frequency equation can be solved from equations (35) and (36), resulting in

$$\frac{\tan(\beta d)}{\tan(\alpha d)} = -\frac{(\xi^2 - \beta^2)^2}{4\alpha\beta\xi^2}. \tag{38}$$

Equations (30), (37), and (38) define the dispersion of the eigenmodes of a suspended plate, an infinite set of modes depending on the thickness of the plates. The lowest Lamb modes along with the SH-modes for a 300 nm SiN film are shown in Figure 2. Only these type of waves can propagate with straight wave fronts within a plate with the boundary conditions set above. [36]

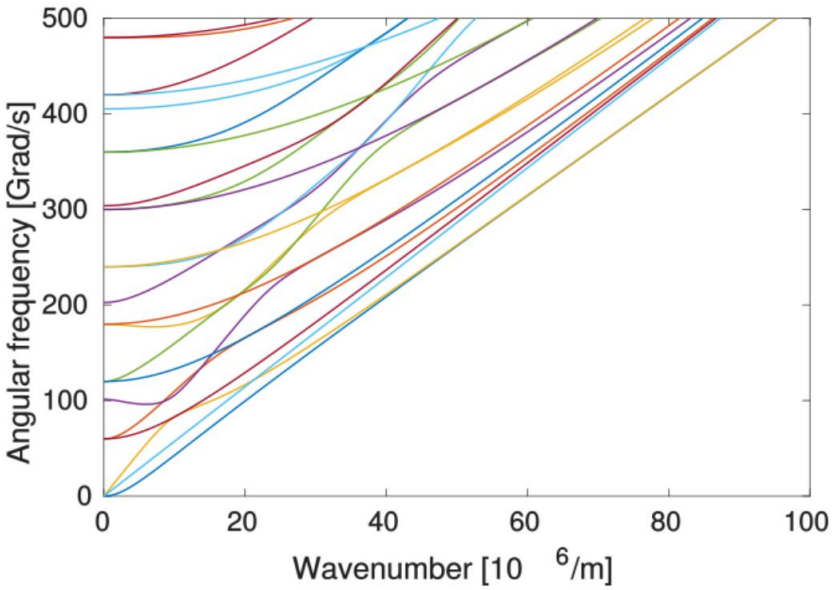

Figure 2. The lowest wave modes of a suspended 300 nm SiN membrane. The image is from Ref. [37], originally calculated by Tuomas Puurtinen.

2.1.3 Emitted phonon power in the ballistic regime

As it turns out, it is possible to model ballistic phonon propagation in a thin film directly with Rayleigh-Lamb theory. Lamb mode-based simulations have been successful in calculations of ballistic phonon transport in SiN membranes [37–39], as well as predicting the emitted phonon power in 2D hole-based PnCs [18, 21].

In an isotropic three-dimensional material the emitted phonon power has the form of the Stefan-Boltzmann law for a phonon gas

$$P(T) = A\sigma T^4, \tag{39}$$

where

$$\sigma = \frac{\pi^5 k_B^4}{15h^3\Sigma(e_i/c_i^2)}, \tag{40}$$

where h is the Planck constant, and $\Sigma(e_i/c_i^2)$ is a summation of radiator emissivities e_i and different phonon mode speeds of sound c_i [39].

When approaching a two-dimensional case the calculation becomes much less trivial, and Lamb modes are required for calculating the emitted phonon power. in the ballistic regime, for a heater on a 2D membrane the emitted phonon power is given

by [24]

$$P(T) = \frac{1}{(2\pi)^2} \sum_j \oint_\gamma d\gamma \int_K d\mathbf{k} \hbar \mathbf{k} \omega_j(\mathbf{k}) n_B \frac{\partial \omega_j}{\partial \mathbf{k}} \cdot \hat{\mathbf{n}}_\gamma \Theta \left(\frac{\partial \omega_j}{\partial \mathbf{k}} \cdot \hat{\mathbf{n}}_\gamma \right). \tag{41}$$

Here γ is the heater surface perpendicular to the membrane, $\omega_j(\mathbf{k})$ is the phonon dispersion relation, n_B is the Bose-Einstein distribution, the term $\partial\omega_j/\partial\mathbf{k}$ is the phonon group velocity, and the step function Θ ensures that only the outward flowing waves with wave vectors $\mathbf{k} \cdot \hat{\mathbf{n}}_\gamma$ are taken into account. Because only the modes parallel to the surface are considered, the model does not perfectly describe a scenario where the phonons are emitted from a heater on top of the sample surface. A more accurate model

$$P(T) = \frac{1}{(2\pi)^2} \sum_j \oint_\gamma d\gamma \int_K d\mathbf{k} \hbar \mathbf{k} \omega_j(\mathbf{k}) n_B \left| \frac{\partial \omega_j}{\partial \mathbf{k}} \right|, \tag{42}$$

developed for [37], was used in the simulations included in this work. The improved model takes into account the wave vectors emitted radially from the heater. Essentially, the difference between the models is a $\pi/2$ multiplier.

If the membrane is thin and the temperature is low, determined by the condition $Td \ll \hbar c_t / 2k_B$, the phonon power can be analytically solved for the fully 2D limit as [38, 39]

$$P_{2D}(T) = \frac{l\hbar}{2\pi^2} \left[\left(\frac{1}{c_t} + \frac{1}{c_s} \right) \Gamma(3)\zeta(3) \left(\frac{k_B T}{\hbar} \right)^3 + \sqrt{\frac{2m^*}{\hbar}} \Gamma\left(\frac{5}{2} \right) \zeta\left(\frac{5}{2} \right) \left(\frac{k_B T}{\hbar} \right)^{5/2} \right], \tag{43}$$

where Γ is the gamma function, ζ is the Riemann zeta function, and m^* is the effective mass of the antisymmetrical Lamb mode

$$m^* = \hbar \left[2c_t d \sqrt{(c_l^2 - c_t^2)/3c_l^2} \right], \tag{44}$$

where c_s is the speed of sound of the symmetric Lamb mode defined as [38]

$$c_s = 2c_t \sqrt{(c_l^2 - c_t^2)/c_l^2}. \tag{45}$$

With a low enough film thickness the first term in equation (43) becomes negligible, and we are left with a $P \propto T^{5/2}$ dependence.

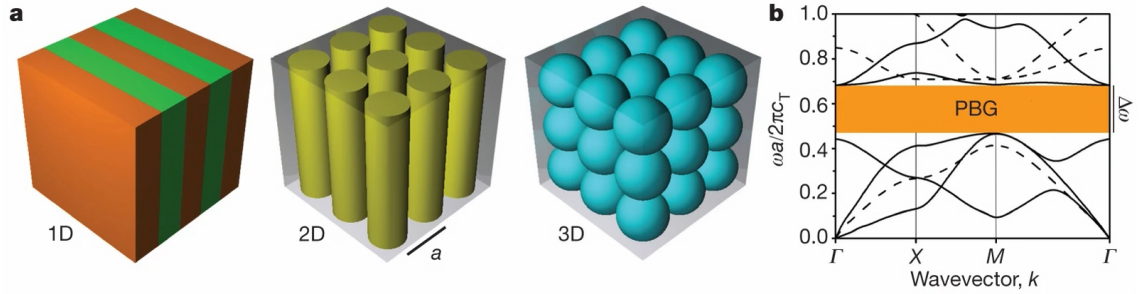

Figure 3. a) Examples of phononic crystals in one, two and three dimensions. **b)** A band gap in the dispersion relation of a phononic crystal. Γ, X and M are points of symmetry in the first Brillouin zone. The figure is reprinted with permission from Ref. [5]. ©2013 Springer Nature.

From the emitted phonon power one can calculate the thermal conductance

$$G = \frac{dP}{dT} \approx \frac{P}{\Delta T}. \tag{46}$$

Note, that thermal conductance G, which has the unit of W/K, is not to be confused with thermal conductivity κ with the dimensions of W/Km. This is analogous to electrical conductance and conductivity. Conductivity is a material constant independent of the geometry, whereas conductance depends on the dimensions of the measured specimen. Within the ballistic regime thermal conductivity is actually not well defined, as the conductance is in that case not dependent on distance.

2.2 Phononic crystals

2.2.1 Overview

A phononic crystal (PnC) is an artificial periodic material which modifies the propagation of phonons, either impeding or enhancing it via some mechanism. The periodicity of the PnC is generally in the same order of magnitude as the wavelength of the phonons which are affected by the crystal, which can be calculated from (23). For example at sub-Kelvin temperatures the dominant thermal phonon frequency is in the order of GHz, which requires a PnC period of $\sim$µm [18].

PNCs can exist in one, two or three dimensions. An example of each is given in Figure 3.a. In principle the materials of a PnC can be anything physically possible. The material of the lattice points can be solid, liquid, gas or a vacuum, and the

surrounding material can be anything capable of supporting the lattice points. For PnCs aimed for thermal transport manipulation, a majority of the devices are simply 2D periodic hole structures in a thin film, the holes filled with air or a vacuum [1, 10, 12].

2.2.2 Coherence and incoherence

The method with which a PnC alters the phononic properties can generally be divided into two categories: coherent and incoherent. For incoherent mechanisms, the phonons scatter diffusely from interfaces and surfaces. This backscattering reduces the number of transported phonons, which effectively reduces the mean free path and results in the reduction and thermal conductance [19, 40, 41]. It is rather widely accepted in the field that for 2D PnCs which affect the heat transport at high temperatures (above $T \approx 10$ K), the thermal conductivity reduction is dominated by incoherent effects [18–20, 40, 41].

When considering incoherent phononic crystals, the essential question is whether a phonon can pass through the lattice. Contrary to coherent scattering where wave phenomena such as interference are essential, with incoherent scattering a phonon can be considered to be purely particle-like. For a fully incoherent scenario the transmitted phonon power per unit are can be calculated from [19, 21, 42]

$$\frac{P}{A} = \frac{1}{4}\langle\tau\rangle \sum_i \int d\omega c_i g_i(\omega)\hbar\omega n_B, \tag{47}$$

where $\langle\tau\rangle$ is the average phonon transmission probability, and c_i and $g(\omega)$ are the speed of sound and the density of phonon states of the mode i, respectively. The summation is over the three bulk phonon modes, two transverse and one longitudinal. The transmission probability depends on the geometric parameters of the PnC and the proportion of specular scattering. Here the phonon modes are not modified by the film thickness, so unlike in equation (43) the temperature dependence would always correspond to a 3D case, equation (39), if the effective mean free path is temperature independent.

In a hole-based structure with diffuse surface scattering, a greater reduction of phonon transmission is induced in a smaller period structure [19, 21], as for smaller periods the "neck" between the holes becomes more narrow. The smaller period

introduces more possible backscattering points for diffusely scattered phonons, as is explained in more detail in Ref. [19].

As discussed in Section 2.1.1, for coherent effects to play a significant role, the phonon transport is required to be ballistic, and the scattering from interfaces needs to be specular. For the majority of coherent phonon manipulation, the physical principle is that phonons Bragg scatter from the periodic lattice with a similar periodicity to the phonon wavelength. The Bragg condition, which gives the constructive interference angles, is given by [28]

$$n\lambda = 2d \sin\theta, \tag{48}$$

where n is an integer, d is the distance between lattice planes and θ is the angle of the incoming waves. The Bragg scattered wave-like phonons then interfere with each other either destructively or constructively. This alters the dispersion relation, creating band gaps in the destructive case, which prevent a phonon with a given frequency from propagating. An example of this is given in Figure 3.b. If the interference is constructive, the phonon DOS can actually increase in certain frequencies, even enhancing the thermal conductivity [24, 43].

As the Bragg condition requires the wavelength to be roughly in the same order of magnitude as the periodicity, one can explore the possibility of achieving Bragg-like interference with room temperature phonons. Using equation (23) we have $\lambda_{dom} = 0.6$ nm at $T = 300$ K in SiN. For Bragg scattering to possess a significant role, the periodicity would have to be of the order of 1 nm. This, along with the required level of surface roughness, is not possible to achieve with current fabrication methods.

2.2.3 Hole-based phononic crystals

For 2D phononic crystals, the majority of research conducted on thermal transport control has been done with hole-based PnCs, both in the coherent and incoherent regime [1, 10]. At room temperature, significant reductions in thermal conductivity have been achieved. In a numerical study by Xie et al.. [41] the thermal conductance of PnCs in silicon with a period in the order of 60 - 100 nm with a varied filling factor was calculated in a temperature range of 50 - 300 K. The simulations were based on Boltzmann transport theory, so incoherent propagation was assumed. The thermal conductivity was significantly reduced, and the simulation was in agreement with experimental data. Here the reduction of thermal conductivity was not attributed

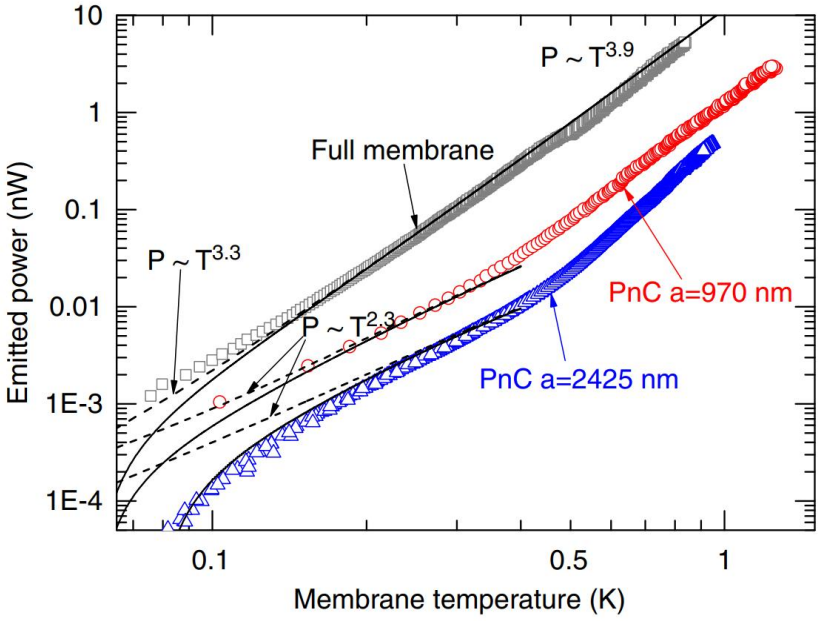

Figure 4. Emitted phonon power as a function of temperature for a 485 nm SiN membrane and two PnCs fabricated on a membrane of the same thickness. The solid lines represent the theoretical results for each case. Figure reprinted from Ref. [18] with permission. ©2014, The Author(s).

to increased number of Umklapp processes which would be dominant in an uniform film, but the reduction was caused by an increase in diffuse surface and boundary scattering caused by the holes.

Thermal conductivity κ of hole-based PnCs in room temperature has been measured for example by Hopkins et al.. [44]. In the study the thermal conductance of a PnC with $a = 500$ nm on a 300 nm thick single crystalline Si film was measured to be as low as 4.81 ± 1.0 W/Km, which is more than an order of magnitude less than the value for an unaltered Si film of the same thickness, 148 W/Km. In the model used by the authors the reduction was not covered by only diffusive scattering, but also a reduction in the phonon DOS was observed in a simulation generated to explain the result.

On the other hand, Anufriev, Maire and Nomura [40] conducted a similar experiment for 80 nm thick single crystalline Si PnCs with a period of 160 - 280 nm with square, hexagonal and honeycomb lattices. The experiment was performed in 4 K and 300 K. The 4 K experiment showed a larger decrease in κ, attributed to coherent effects beginning to have significance. In 300 K the largest reduction was close to 50 %,

but the smaller reduction can be explained by 80 nm Si film already possessing a rather low κ of 58 W/Km. The reduction of κ at 300 K was entirely attributed to incoherent effects, the reduction originating from surface scattering caused by the holes.

At sub-Kelvin temperatures, experimental results have been obtained of coherent thermal conductance reduction by hole-based PnCs. In a study by Zen et al.. [18] finite element method (FEM) simulations were used to predict a period which would introduce a band gap, and a PnC device with these parameters was fabricated. The emitted phonon power was measured with SINIS-thermometry. The results are presented in Figure 4, where a thermal conductance reduction of over an order of magnitude is observed. Based on the results it was concluded that the decrease of thermal conductance is caused not only by the band gap, but also the reduction of group velocities and the DOS. Further theoretical investigation of this is presented in an article by Puurtinen and Maasilta [24], where 300 nm thick PnCs with a constant filling factor and a period ranging from 62.5 nm to 8 μm were studied with FEM simulations in a temperature range of 0.1 - 400 mK. The largest thermal conductance reduction was observed with the largest period.

In Ref. [18] most of the thermal conductance reduction was attributed to the decreased group velocity. In a further study [21], PnCs with a similar thickness and filling factor with periods of 4, 8 and 16 μm were studied with SINIS-thermometry. Here even lower thermal conductances than in [18] are measured, the lowest thermal conductance of 3.2 pW/K at 0.2 K being achieved with the 8 μm period. A fully coherent theory would predict the largest period to have the largest reduction, so here it is concluded that with the 16 μm period the coherent theory starts to break down as incoherent effects begin to have significance.

A numerical study by Anufriev and Nomura [45] also provides a reduction of thermal conductance around one order of magnitude compared to an unpatterned film. Here periods of 80 nm, 160 nm and 320 nm are studied at 0-2 K, the largest period again yielding the greatest reduction. The effects of different lattice geometries (square, hexagonal and honeycomb) are also calculated. The impact of the lattice geometry was rather weak compared to other parameters, but the largest reduction was in the case of a honeycomb lattice.

Also, as was noted in section 2.2.2, hole-based PnCs in the coherent regime with small

enough period can actually increase thermal conductivity. This was also studied in [24]. The enhancement seems to be resulting from an increase of the DOS with a small enough period at low frequencies, and appears to peak with a factor of ~ 3 at around 300 mK with the smallest studied period of 62.5 nm. The enhancement seems to disappear with a large enough period. The thermal conductance enhancement is also observed in a numerical study by Anufriev and Nomura [43]. Here FEM simulations are also used, but here the thermal conductance seems to grow limitlessly with a smaller period instead of peaking. According to Puurtinen and Maasilta the difference is caused by an erroneous assumption of constant group velocities on a constant energy surface in [43], as 2D PnCs are not isotropic.

2.2.4 Local resonance

Coherent dispersion manipulation in 2D PnCs with Bragg scattering is a relatively well understood method, even in the thermal phonon regime. A somewhat less studied coherent method is the local resonance-based dispersion manipulation, where in the 2D-case the band gaps are created with locally resonant structures on top of a membrane.

The following examination is based on an example by Laude in [4]. We consider the behaviour of a single massive resonator on top of a 1D waveguide, such as a suspended nanowire, with only one allowed frequency mode $\omega = \pi c/d$, where d is the thickness of the waveguide. The resonator can be described as a forced harmonic oscillator

$$\varkappa u + M\frac{\partial^2 u}{\partial t^2} = Fe^{i\omega t}, \tag{49}$$

where u is the displacement, $\varkappa$ is the stiffness of the material, and F is the force on the oscillator. If the motion is harmonic ($u = \bar{u}\exp(i\omega t)$), the oscillation amplitude $\bar{u}$ can be written as a function of the resonance frequency $\Omega = \sqrt{\varkappa/M}$ as

$$\bar{u} = \frac{F}{M}\frac{1}{\Omega^2 - \omega^2} = \frac{F}{M}L(\omega), \tag{50}$$

where $L(\omega)$ is the Lorenzian spectral line shape. Here clearly $\bar{u} \to \infty$ as $\omega \to \Omega$. If we set $x_1 = 0$ at the location of the resonator, we can write the field far from and on the left and right of the resonator as a superposition of the left and right propagating

guided waves

$$p_0(\mathbf{x}) = \begin{cases} \psi_0(x_2)(A_1 e^{-ikx_1} + B_1 e^{ikx_1}), & \text{if } x_1 \ll 0 \\ \psi_0(x_2)(A_2 e^{-ikx_1} + B_2 e^{ikx_1}), & \text{if } x_1 \gg 0, \end{cases} \tag{51}$$

where A and B are amplitudes, $k = \pm\omega/c$, and $\psi_0(x_2)$ is the transverse mode distribution. $\psi_0(x_2)$ can be considered a constant in the 2D case, where x_2 is the direction orthogonal to the waveguide in the direction of the resonator.

Equation (51) however does not hold close to the resonator. In the resonators vicinity, the boundary conditions are modified so that field inside the waveguide induces a driving force on the resonator, given a frequency near the resonance frequency. This motion of the resonator changes the equilibrium of the waveguide locally. In an idealisation where the resonator is in contact with the waveguide in only one point $x_1 = 0$, where the force density is proportional to the Dirac delta $\delta(x_1)$, this localised excitation results in bound evanescent modes in the waveguide. The field of this second transmission channel is

$$p_1(\mathbf{x}) = \begin{cases} C_1\psi_1(x_2)e^{\alpha x_1}, & \text{if } x_1 < 0 \\ C_2\psi_1(x_2)e^{-\alpha x_1}, & \text{if } x_1 > 0, \end{cases} \tag{52}$$

where $\alpha = \sqrt{(\pi/d)^2 - (\omega/c^2)}$, and $\psi_1(x_2) \propto \cos(\pi x_2/d)$ is the transverse mode distribution for evanescent modes in the waveguide. For the whole waveguide, except for $x_1 = 0$, the total field is now $p(\mathbf{x}) = p_0(\mathbf{x}) + p_1(\mathbf{x})$. As the two modes are orthogonal, we obtain the conditions

$$A_1 + B_1 = A_2 + B_2, \tag{53}$$

$$C_1 = C_2. \tag{54}$$

We assume the field is continuous at the connection point. However, $\partial p/\partial x_1$ is not continuous at at the junction due to p_1 being discontinuous. The jump of the derivative $\partial p/\partial x_1$ will be written as

$$\left[\frac{\partial p}{\partial x_1}\right]_{0+} - \left[\frac{\partial p}{\partial x_1}\right]_{0-} = L(\omega)\beta(x_2)p(0,x_2). \tag{55}$$

This is obtained by integrating the waveguide wave equation which is subjected to a force density $L(\omega)\beta(x_2)p(x)\delta(x_1)$, where $\beta(x_2)$ is a stress distribution with a cross-section dependence created by the force density on the resonator, the shape of which is given by $L(\omega)$. This can be interpreted as a field distribution $p(\mathbf{x})$ at the junction setting the resonator into motion creating a stress distribution, a function of x_2. By applying this for the two modes, we obtain the relations

$$ik(-A_2 + B_2) - ik(-A_1 + B_1) = L(\omega)(\beta_{00}(A_1 + B_1) + \beta_{01}C_2) \tag{56}$$

$$-\alpha(C_1 + C_2) = L(\omega)(\beta_{10}(A_1 + B_1) + \beta_{11}C_2), \tag{57}$$

where

$$\beta_{ij} = \int dx_2 \beta(x_2)\psi_i(x_2)\psi_j(x_2). \tag{58}$$

Essentially, the discontinuity couples the two modes at the junction point. As we have created two equations for the amplitudes of $\psi_{1,2}$ from one equation, we must make sure the determinant of the matrix β_{ij} vanishes by adding a compatibility relation $\beta_{00}\beta_{01} - \beta_{01}\beta_{10}$.

By solving the equations (56) and (57), and by defining the terms $\gamma_{0j} = L(\omega)\beta_{0j}/(2ik)$ and $\gamma_{1j} = L(\omega)\beta_{1j}/(2\alpha)$, we obtain the solution matrix relating the incoming and outgoing amplitudes

$$\begin{pmatrix} A_2 \\ B_1 \\ C_2 \end{pmatrix} = \begin{pmatrix} t & r \\ r & t \\ s & s \end{pmatrix} \begin{pmatrix} A_1 \\ B_2 \end{pmatrix}, \tag{59}$$

where r is the reflection coefficient, t is the transmission coefficient and s is the proportion of the incoming amplitude stored in the evanescent wave. The coefficients can be written explicitly as

$$t = \frac{1 + \gamma_{11}}{D}, \tag{60}$$

$$r = t - 1, \tag{61}$$

$$s = \frac{\gamma_{10}}{D}. \tag{62}$$

Here $D = (1 + \gamma_{00})(1 + \gamma_{11}) - \gamma_{01}\gamma_{10} = 1 + \gamma_{00} + \gamma_{11}$ with the compability condition applied. ŧFar from the resonance condition γ_{ij} are negligible, and $t = 1$. The

condition for $t = 0$, and therefore $r = 1$, is given by $1 + \gamma_{11} = 0$, which occurs when

$$\omega^2 = \Omega^2 + \frac{\beta_{11}}{2\alpha}. \tag{63}$$

This tells us that even with a small coupling strength, the transmission can be cancelled with a frequency in the close vicinity, but not exactly equal to the natural frequency of the oscillator Ω.

This can be expanded for a case with a 1D periodic lattice of resonators on the waveguide, with periodic Bloch boundary conditions

$$p_0(a/2, x_2) = e^{iKa} p_0(-a/2, x_2), \tag{64}$$

where K is the Bloch wave vector [28] and a is the lattice constant. By solving the transmission matrix

$$\begin{pmatrix} A_2 \\ B_2 \end{pmatrix} = \begin{pmatrix} \frac{t^2 - r^2}{t} & \frac{r}{t} \\ -\frac{r}{t} & \frac{1}{t} \end{pmatrix} = \begin{pmatrix} A_1 \\ B_1 \end{pmatrix} \tag{65}$$

with the eigenvalues of $\lambda = e^{-iKa}$, the dispersion relation for the system becomes

$$\cos(Ka) = \cos(ka) + i\frac{r}{t}\sin(ka) = \cos(ka) - \frac{L(\omega)\alpha\beta_{11}}{2\alpha\beta + L(\omega)k\beta_{22}}\sin(ka). \tag{66}$$

As $r \to 0$ the relation reduces to $K = \pm k$, and we again have the unaltered dispersion of the waveguide mode, where the resonators do not affect the wave propagation. When approaching the resonance, the second term in equation (66) becomes dominant. Around the resonant frequency, when $|\cos(Ka) > 1|$, K becomes complex, which creates a transmission zero, or a band gap, in the dispersion relation. This is illustrated in Figure 5.

2.2.5 Pillar-based phononic crystals

Phononic crystals for which local resonance is the phenomenon creating the band gaps are generally referred to as locally resonant phononic crystals. The first locally resonant PnC, created by Liu et al. in 2000 [22], was a structure where the resonators were lead balls coated with silicon rubber in a 3D lattice in an epoxy matrix [22]. The lead balls could move rather freely in the rubber, and band gaps caused by resonance were observed around 1 kHz. However, arguably the most common type of

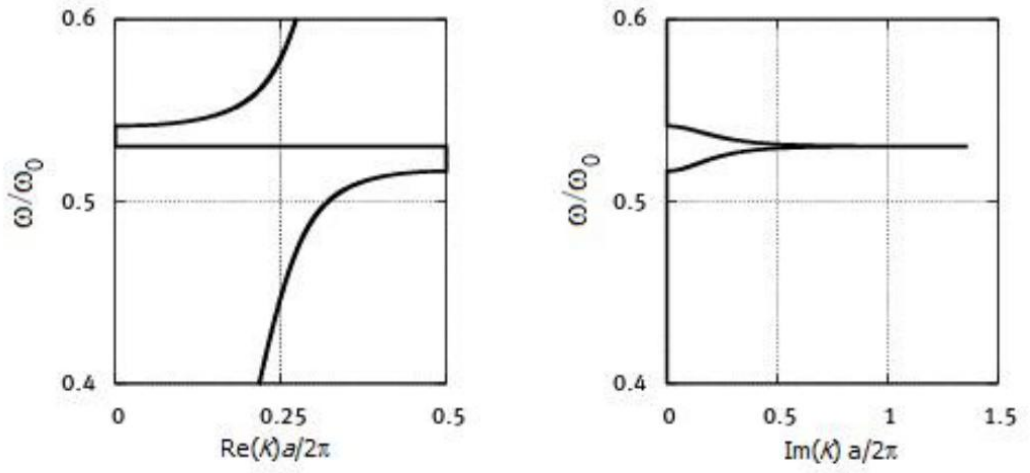

Figure 5. The real and imaginary parts of the dispersion relation of a periodic array of pillars on a 1D waveguide around the resonance frequency ω_0.

locally resonant PnCs are pillar-based PnCs, 2D-crystals where the locally resonant structures are pillars on top of a film, a bulk material, or a suspended beam or a wire.

For the pillar-based PnCs, the sonic frequency range of acoustic phonons is relatively well studied, and most of the theoretical and especially experimental studies are focused there. The acoustic band gaps created by local resonances can exist in frequencies two orders of magnitude lower than the Bragg gap would be for a PnC of identical periodicity [10, 46]. Locally resonant PnC structures, much like like hole-based PnCs [5], can also be utilised in waveguiding applications [47], where phonons with a given frequencies are only allowed to propagate through a certain path. More on the low frequency pillar-based PnCs and their applications can be found in the review article by Pennec et al. [10], and the book by Laude [4].

In a number of theoretical studies it is stated that both the local resonances and Bragg scattering contribute to to the band gap formation in pillar-based PnC [48–52]. An example of this is given in Figure 6. This is supported by the experimental evidence by Achaoui et al. [53], where periodic and non-periodic arrays of pillars were studied. The PnC was fabricated on $LiNbO_3$, the piezoelectric properties of which were used for measuring the phonon transmission. As can be seen in Figure 7, in the case of a PnC with a honeycomb lattice, there is an observable Bragg band gap, which disappears when the periodicity is destroyed. However, a gap created by the local resonances persists for both cases. This also implies that periodicity is not

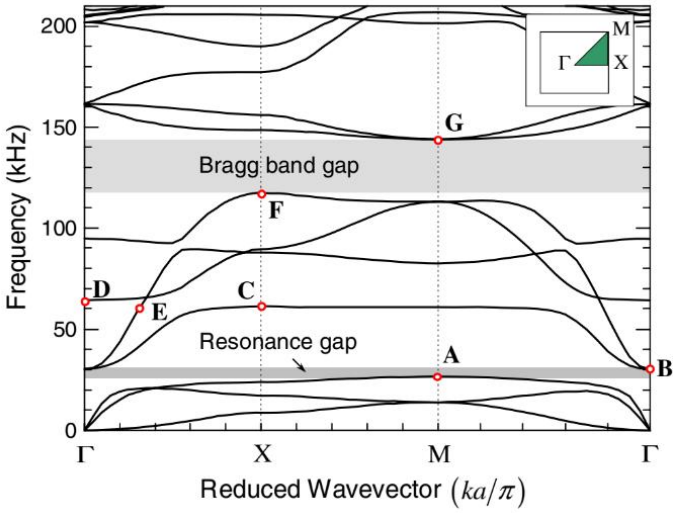

Figure 6. Dispersion relation for a pillar-based PnC, where a Bragg scattering and a local resonance induced band gap are both visible. Here the material of the substrate and the pillars is steel, the pillars being cylindrical with a narrower "neck" between them and the substrate. The parameters for the PnC were $a = 10$ mm, height $h = 4$ mm, pillar radius was $r = 4.5$ mm and the membrane thickness was $d = 1$ mm. Figure reprinted from Ref. [52] with permission. ©2011 IOP Publishing, Ltd.

needed for local resonance based dispersion relation manipulation, but the periodicity can increase the effect by creating additional band gaps. In [54] Achaoui et al. again observed two band gaps: a high frequency one in the range of a Bragg gap, and a lower frequency gap attributed to local resonances. Based on the theoretical studies by Pourabolghasem et al. [50], the local frequency band gap can also exist in higher frequencies than the Bragg gap.

In Figure 7, the crystal with a hexagonal lattice exhibits a transmission differing from the honeycomb lattice around the local resonance band gap. This would indicate that the lattice type has a role even in the locally resonant case. There exist a few theoretical studies on the matter: If calculations are performed with a semi-infinite substrate, such as simulations by Khelif, Achaoui and Aoubiza [48], the locally resonant band gaps show marginal dependence on the lattice type. When the calculations are done on a finite slab of material in a vacuum, where the membrane waves are Lamb waves and the surface waves are Rayleigh waves, surface waves similar to Lamb waves, a stronger dependence on the lattice type appears. This was the case in a numerical study by Hsu [52]. This dependence is caused by the

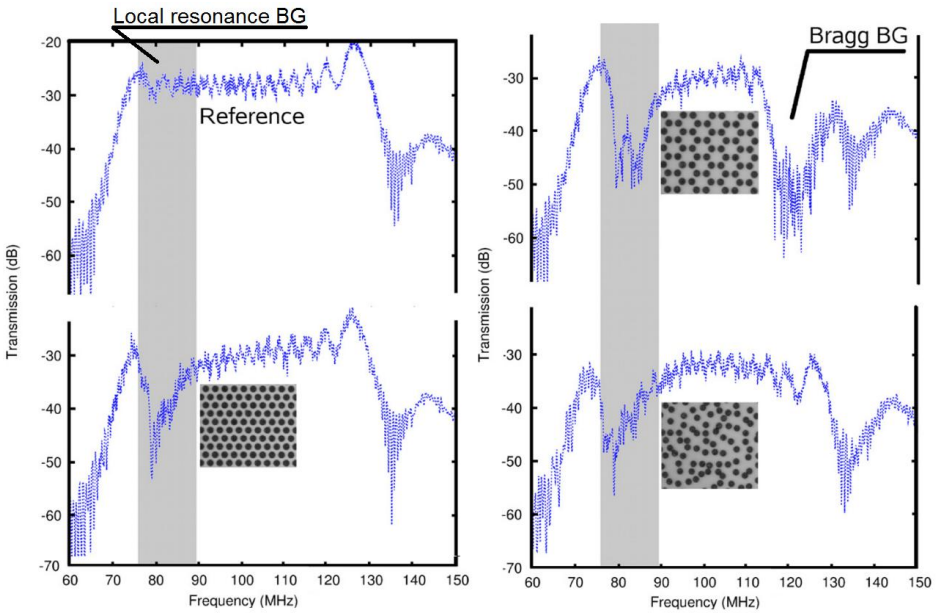

Figure 7. Transmission as a function of frecuency for pillar-based phononic crystals of different lattice types in the MHz regime. Figure reprinted from [53], with the permission of AIP Publishing.

coupling of adjacent resonators, so it is fair to assume that the lattice type would affect the coupling. In both articles the simulations were conducted using FEM.

Obviously, other geometrical parameters of the PnC also affect the dispersion. The pillar mass, which depends on size and the density of the material, partly determines the resonant frequency. A PnC with cylindrical pillars of silicon on top of a silicon substrate were studied with FEM simulations by Khelif et al. [49]. It was discovered that the ratio of pillar height and the lattice period h/a was a parameter for which the location of the local resonances in energy was the most sensitive to. However, this could also be interpreted as a sensitivity to the resonator mass or the filling factor.

2.2.6 Pillar-based phononic crystals at thermal frequencies

In the past few years, a number of different approaches have been adopted in simulating the thermal transport in pillar-based PnCs. One of the earliest proposals of using locally resonant PnCs in reduction of thermal conduction was by Hussein and Davis in 2014 [26]. Here lattice dynamics simulations in silicon were used to obtain the phononic band structure, and the Callaway-Holland model [55] was used to predict the thermal conductivity. The frequency range was in the THz, corresponding to the dominant phonon frequencies at room temperature. The film thickness was 2.72 nm and the period was 3.26 nm, which would allow for coherent effects to take place in an ideal structure. The simulations showed a significant alteration to the DOS, group velocity and dispersion, resulting in a reduced thermal conductivity down to 50 %.

Molecular dynamics simulations, a computational method similar to lattice dynamics, were used by Honarvar and Hussein [56] to analyze the phononic spectrum of a pillar-based structure with Si pillars on a suspended Si membrane in the THz range. Based on the dispersion relation, the structure exhibited numerous local resonances, which caused a reduction in the phonon group velocity, and subsequently in thermal conductivity. The simulation results were consistent with earlier lattice dynamics simulations in Ref. [26], yielding a reduction of 50 %. Continuing this work, another article with room temperature molecular dynamics simulations by Honarvar, Yang and Hussein [57] discussed the effects of the pillar and unit cell size. The length scale in both of these studies was also quite small, in the order of 1 nm to 10 nm. According to the simulations, the thermal conductivity is reduced with increasing pillar height and decreasing film thickness and pillar width. Wei et al. [58] also used molecular and lattice dynamics in the THz frequency range and nm size range to obtain a thermal conductance reduction of up to 71.4 %. The pillars were Si on a suspended Si thin film.

Molecular dynamics was also utilised by Xiong et al. [59] to calculate phonon propagation in SiGe alloy nanowire with pillars on one side, or pillars symmetrically on two or four sides of the wire. These simulations were also done in the THz regime, the wire thickness was 4.34 nm, and the resonator period was varied between 2.17 and 7.60 nm. The increase of pillars on different sides of the wire appeared to decrease the thermal conductivity, and the conductivity also decreased with a smaller

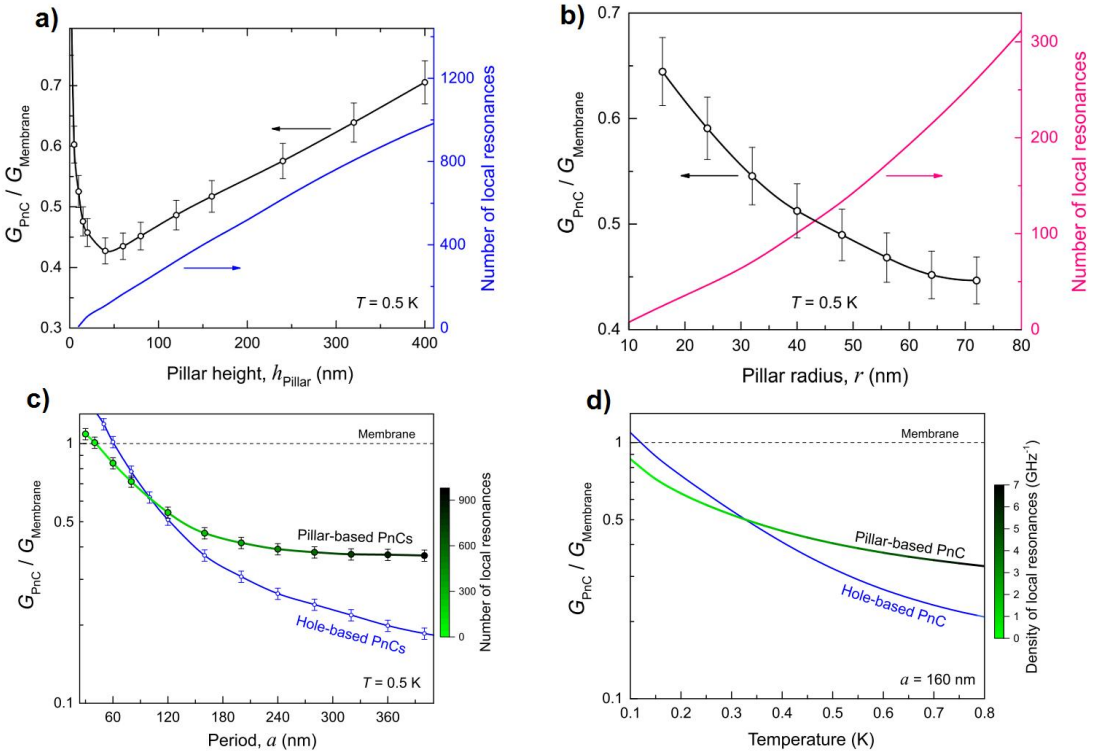

Figure 8. The behaviour of the thermal conductance of pillar based hexagonal phononic crystals compared to the thermal conductance of an unmodified film as a function of **a)** pillar height, **b)** radius, **c)** period and **d)** temperature. In **c)** and **d)** the values are also compared with the values of a hole-based PnC with similar parameters. The film thickness is 80 nm, and the constant values in the graphs where the value itself is not under study are $T = 0.5$ K, $a = 160$ nm, $h = 80$ nm, and $r/a = 0.4$. Figures reprinted with permission from [25]. ©2017 by the American Physical Society.

period, resulting in a similar $\sim 50\,\%$ decrease as in Ref. [26]. A similar structure, a silicon nanowire with periodic rectangular "wings", was studied by Anufriev and Nomura [60], although here the simulations were done in the coherent regime at 0.5 K, and using continuous elasticity theory and FEM. Due to the low temperature, the wing period was 300 nm, and the phonon frequencies were < 100 GHz. A reduction in thermal conductance of $\sim 50\,\%$ was again obtained. However, here most of the thermal conduction reduction was attributed to the periodicity, and the effect of local resonances was considered weaker.

A rather extensive numeric study on the effects of different parameters to the thermal conductance was conducted by Anufriev and Nomura in 2017 [25], where FEM

simulations were used to obtain the dispersion relations. Some of the results of the article for a hexagonal lattice of cylindrical pillars are presented in Figure 8. As in previously discussed studies, here the maximum reduction of thermal conductance is also close to 50 %. The effects of different lattice geometries were also studied, and a honeycomb lattice resulted in a 10 % decrease in thermal conductance compared to the hexagonal lattice, while a square lattice resulted in a 20 % decrease. However, these reductions were rather small compared to the effects of other parameters. A hybrid structure of pillars and holes was also investigated, yielding a 21 % greater thermal conductance reduction than a hole-based PnC. This is argued to originate from the additional flattening of the band structure and a strongly reduced group velocity.

Yet another molecular dynamics based study by Honarvar and Hussein in 2018 [61] at room temperature frequencies resulted in a thermal conductance reduction of factor 130. The studied system was once again a suspended Si membrane of thickness $\leq$ 10 nm, with Si pillars on one or both sides. For the largest reduction the film thickness was 9.78 nm, and the pillar height and width were 6.13 nm. For most of the previous THz studies, the thermal conductivity reduction quickly decreased with a larger structure. This is not the case here. The difference was accounting for the vibron (hybridization between pairs of the wave-number-independent vibration modes) compensation, meaning that the resonator sizes were increased with a higher rate than the base membrane, when the size of the unit cell increases. This leads to a stronger coupling between the phonons and the localised resonance modes than with other numeric studies, where the method of obtaining larger reductions was mere parameter optimisation.

Pillar-based PnCs with a period of the order of 100 nm have been successfully fabricated [51, 62, 63]. Sledzinska et al.. [62] fabricated Al pillars with a period of 500 on a suspended Si film. In a study by Graczykowski et al.. [51] the pillar material was Au, and a study by Yudistira et al.. [63] had pillars of $LiNbO_3$ on a 3D substrate of the same material. In all of these studies the existence of band gaps in the GHz frequencies was experimentally confirmed by Brillouin light scattering.

The heat capacity of a PnC consisting of Si pillars on bulk Si crystal, fabricated with reactive ion etching from a single wafer, was measured by Iskandar et al. [64] in the temperature range from 3 to 300 K. The heat capacity of the specimen was altered,

either decreased or increased depending on the height, diameter and the slope of the pillar walls.

In a room temperature study by Anufriev, Yanagisawa and Nomura [65], the thermal conductivity of a nanobeam with a periodic arrangement of Al pillars was measured to be 20 % lower than the unaltered wire. The beam width was 840 nm, the thickness was 70 nm, the studied pillar diameters were 229.5 nm, 243.5 nm and 335 nm, and the period was 560 nm. The measurements were done using Time-domain thermoreflectance (TDTR), and the largest decrease in thermal conductivity was caused by the largest pillar diameter. The authors concluded that the thermal conductivity reduction was caused by diffusive scattering from the Al-Si interface, as the temperature was too high for coherent effects to play a role.

Incoherent thermal conductance reduction can also be achieved with other pillar-like structures. Huang et al. [66] measured the thermal conductance of a 50 nm thick Si nanobeam using TDTR, with cone-like Si structures with the structure size in the order of tens of nanometers on the surface. The cones had a random arrangement and they were of unequal size. The measurement temperature range was 4 K - 295 K, and the lowest thermal conducitivity was 58 % of the smooth beam thermal conductivity at 4 K. As normally the proportion of the specular scattering would increase at lower temperatures, here the cones increase the phonon scattering decreasing the amount of specular scattering events and "trapping" the phonons, thus decreasing the thermal conductance. The experimental data fit to this model.

A research paper from 2019 by Zhang et al. [67] describes a 56 % thermal conductance reduction of a suspended 500 nm SiN membrane by a pillar pattern at 100 mK. A Transition edge sensor (TES) was surrounded by an array of pillars in a hexagonal lattice or rings, the period being either 7 or 10 µm with a 1/3 or a 2/3 filling factor. The materials for the features were Au ($h = 270$ nm), a normal metal, and Mo ($h = 54$ nm), a superconductor. The best results were achieved with a 7 µm period of Au pillars with a 2/3 filling factor, and Au rings with a 7 µm spacing and a 2/3 coverage. Here the suggested mechanism of thermal conductance reduction was diffusive scattering from the metal features, in other words incoherent scattering. The thermal conductance was obtained by analysing the IV-characteristics of the TES.

2.2.7 Comparison of pillar- and hole-based phononic crystals

Most numerical studies yield a reasonably consistent ~ 50 % reduction in thermal conductivity for pillar-based PnCs, both in the sub-Kelvin region and at room temperature, with the one outlier of Ref. [61] producing an immensely greater reduction. The ~ 50 % was also obtained for the single experimental result at sub-Kelvin temperatures. With hole-based PnCs, reductions of the order of 100 have been routinely achieved with numeric studies, and also with a few experimental ones. Figure 8 presents an example of calculated pillar- vs hole-based PnC thermal conductance reductions. However, with the results of Ref. [61], it may be possible to experimentally reach similar reductions for pillar-based structures as for hole-based PnCs with careful parameter planning.

As both Bragg and local resonances play a role in the coherent regime for pillar-based PnCs, they may be more versatile in phonon dispersion manipulation. Combining these effects could lead to a wider band gap or a larger affected frequency range. Also, as was suggested in Ref. [25], pillars and holes can also be combined to form a single structure. These hybrid structures can exhibit a larger thermal conductance reduction than a simple hole-based PnC. Perhaps an even larger reduction can be achieved by combining pillars and holes with different parameters.

2.3 SINIS thermometry

In this work, a SINIS-thermometer (superconductor-insulator-normal metal-insulator-superconductor) was used in conjunction with a SNS-heater (superconductor-normal metal-superconductor) to measure the emitted phonon power. A SINIS-junction consists of two NIS tunnel junctions in series. A single NIS-junction can also function as a thermometer, but a SINIS-junction is more sensitive. If the junction is biased with an appropriate constant current, voltage over the junction becomes sensitive to changes in temperature at the temperature range roughly from 100 mK to below the critical temperature of the superconductor. The range and sensitivity can also be tuned by changing the bias current. [68, 69]

The advantages of using SINIS-junctions as a thermometer include low self-heating, high sensitivity in the range of the thermometer, and compact size so that they can be easily fabricated on a given sample. A SINIS-junction can also function as a

heater or an electron cooler [68–70]. The limitations of SINIS thermometry include its limited temperature range and the tendency to break easily due to static charges. The range for the most common type of junctions, where the superconducting metal is aluminium, is approximately 0.1-1 K. For a larger range, for example niobium and niobium nitride based devices have been developed achieving sensitivities at temperatures up to 11 K [70, 71].

2.3.1 Aspects of the BCS Theory of Superconductivity

The phenomenon of superconductivity was first discovered by Heike Kamerlingh Onnes in 1911 in mercury cooled with liquid helium. A microscopic theory for superconductivity was however only devised in 1957 by Bardeen, Cooper and Schrieffer [72], named the BCS theory according to its creators. This chapter will only briefly discuss the primary concepts and results of conventional type I superconductivity, and subjects such as high temperature superconductors are not discussed.

Superconductivity is characterised by two main phenomena: perfect conductivity, or a current without resistance, and the Meissner effect. A material enters the superconducting phase when it is cooled below its critical temperature T_c. For all elemental superconductors $T_c < 10$ K. A sufficiently weak magnetic field is also completely repulsed from the material. This is called the Meissner effect. The length a magnetic field penetrates into a superconductor is referred to as the penetration depth λ. An approximation by London for λ at zero temperature is given by

$$\lambda(0) = \sqrt{\frac{m}{\mu_0 n e^2}}, \tag{67}$$

where n is the density of conduction electrons. For a large enough field H_c the magnetic field completely penetrates into the sample, and superconductivity is lost in type I sueprconductors. The critical temperature and field are approximately related by the empirical law

$$H_c(T) = H_c(0)\left[1 - \left(\frac{T}{T_c}\right)^2\right]. \tag{68}$$

From the existence of a critical field it is apparent that a critical current also exists, where a current in a wire is large enough to induce a magnetic field around the wire

surface equal to the critical field. This can be written as

$$J_c = \frac{1}{\mu_0}\frac{H_c}{\lambda}. \tag{69}$$

[73]

The fundamental idea of the BCS theory is that even a weak attractive interaction between electrons can form bound states of two electrons. The source of this attractive interaction is electron-phonon coupling, where a moving electron polarises the ion lattice by attracting a positive ion, which then in turns attracts an another electron, inducing an effective attraction between the two electrons. These coupled electron pairs are called Cooper pairs. Between the superconducting ground state and a certain energy there are no occupied states, and any quasiparticle excitations exists only above this energy gap, the magnitude of which is equal to half the energy required to break a Cooper pair. The effective size of a Cooper pair, or the smallest possible size of a wave packet, is given by the Pippard coherence length

$$\xi_0 = a\frac{\hbar v_F}{k_B T_c}, \tag{70}$$

where v_F is the Fermi velocity and a is a numerical constant with a value of 0.18 given by the BCS theory. [73]

The magnitude of the energy gap at zero temperature is [72]

$$\Delta = \frac{\hbar\omega_c}{1/\sinh\left[N(0)V\right]}, \tag{71}$$

where $N(0)$ is the normal density of states at Fermi energy, and V is the interaction potential. The ω_c is the critical frequency above which no acoustic phonons exist. With the Debye model, $\omega_c = \omega_D$. The temperature dependence of Δ is given by [72]

$$\frac{1}{N(0)V} = \int_0^{\hbar\omega_c} \frac{\tanh\left[\frac{1}{2}\beta(\xi^2+\Delta^2)^{\frac{1}{2}}\right]}{(\xi^2+\Delta^2)^{\frac{1}{2}}} d\xi, \tag{72}$$

where β is the familiar $(k_B T)^{-1}$, and ξ is the single particle energy relative to the Fermi energy. In the so-called weak coupling limit, which applies to many low temperature superconductors [73], the zero temperature energy gap can be

approximated by

$$\Delta(0) = 1.764\, k_B T_c. \tag{73}$$

The critical field of a bulk specimen at 0 K can also be expressed in term of the BCS energy gap [72]:

$$H_c(0) = \left[\frac{N(0)}{\mu_0}\right]^{\frac{1}{2}} \Delta(0). \tag{74}$$

2.3.2 Andreev reflection

If a current flows from a normal metal to a superconductor, part of the current is immediately converted into a supercurrent at the interface, and a part of the current is carried over to the superconductor as a nonequilibrium quasiparticle charge, which is converted into a supercurrent over a certain diffusion length. The actual proportion of these two conversion mechanisms is dependent on the properties of the barrier and bias voltage[73, 74].

The mechanism where the conversion happens immediately at the interface is called Andreev reflection, and it is generally dominant at interfaces with high transparency. If an electron incoming from the normal metal has an energy of $E > \Delta$, it can pass into the superconductor uninhibited as a quasiparticle, converting into supercurrent after the diffusion length. However, if the energy of an electron is $E < \Delta$, it can not be transferred into the superconductor as a quasiparticle, as the states below Δ are forbidden. With a clean interface, or in the absence of a scattering potential, the electron is reflected back to the normal metal as a hole, which transfers a charge of $-2e$ into the Cooper pair condensate of the superconductor. With a clean interface with E and $k_B T \ll \Delta$, Andreev reflection is the dominant current transfer method across an NS-junction. For a transmission probability $t = 1$, we have reflection probabilities R of [74]

$$r = 1, \quad |E| < \Delta \tag{75}$$

$$r = \frac{E - \sqrt{E^2 - \Delta^2}}{E + \sqrt{E^2 - \Delta^2}}, \quad |E| > \Delta. \tag{76}$$

Also, with Andreev reflection as the prominent method of carrying current across the interface, there is no heat current carried from the normal metal into the superconductor, as no quasiparticles penetrate the interface. [73, 74]

However, in a real life scenario there is often a finite tunnel barrier present, especially in the presence of an oxide layer [73]. This decreases the proportion of Andreev reflection as normal reflection from the barrier becomes more prominent. With $t \ll 1$, the subgap reflection probability has the form [75]

$$r = \frac{t^2\Delta}{4(\Delta^2 - E^2)}, \quad E < \Delta. \tag{77}$$

The proximity effect is a larger scale phenomenon induced by the Andreev reflection. In a contact between a normal metal and a superconductor, Cooper pairs from the superconductor are diffused into the normal metal, and quasiparticle excitations from the normal metal are carried into the superconductor. The proximity effect can be observed as the suppression of a T_c of a superconductor in the presence of a normal metal layer, and inversely as an increase of conductivity in a thin layer of the normal metal. [74]

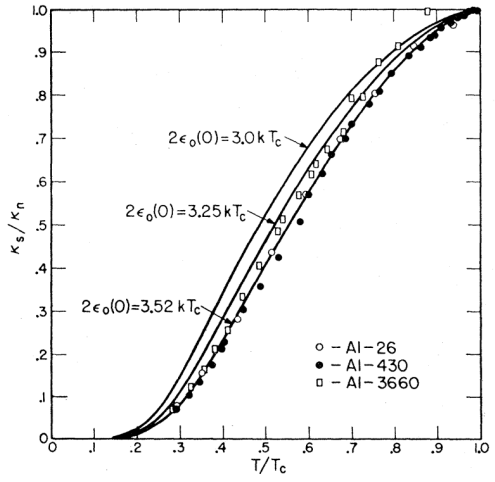

Figure 9. A measured thermal conductance ratio of superconducting K_s and normal metal K_n in Al. The different Al represent different levels of purity, with Al-26 being the most impure with a 0.3 % concentration of copper. Solid lines represent values calculated from BSC-theory with different values for the energy gap. Figure reprinted with permission from [76]. ©1959 American Physical Society.

2.3.3 Phonons in superconductors

As was mentioned earlier, in normal metals the majority of heat is carried by electrons. In superconductors, below the transition temperature the electronic thermal conductivity begins to drop exponentially. On the other hand, in an infinite crystal the phononic thermal conductance increases, although at a slightly lower rate compared to the decrease of the electronic component. As a result, the overall thermal conductance is lowered as a function of temperature, as is shown in Figure 9 [77].

In a metal, or in an interface between a metal and an insulator, electrons can either receive or give out energy to phonons. An electron absorbing or emitting a phonon is illustrated in a Feynman diagram in Figure 10. The mechanism of phonon absorption can be understood as a lattice vibration inducing a change in an electrons momentum, and the phonon emission can be thought as a a change in local charge density induced by an electron, which is then mediated by an elecrostatic interaction into vibrations. As there are no gaps in the density of states for normal metals near Fermi energy, phonons at any energy can be absorbed.

Low frequency phonons at low temperatures do not scatter from superconductors, as the superconducting energy gap prevents phonons with subgap energies from transferring energy to the Cooper pair electrons, leaving the phonon with its initial momentum. This can be easily verified for aluminium at temperatures $T \ll T_c$: The superconducting gap for Al, from equation (73) with a T_c value of 1.196 K [28], is 0.18 meV. The energy of a phonon is $\omega\hbar$. Using the dominant phonon frequency of equation (22) we have $E_{phonon} = 0.068$ meV at 0.1 K, so most of the incoming phonons are not scattered in Al.

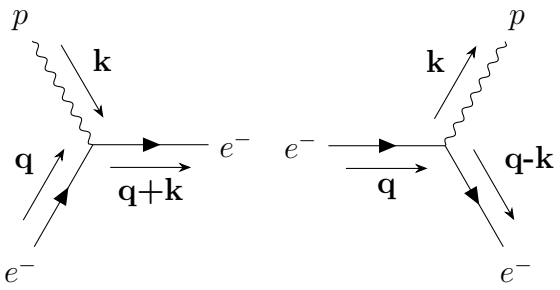

Figure 10. A Feynman diagram of an electron absorbing (left), and emitting a phonon (right). **k** and **q** are the phonon and electron wave vectors, respectively.

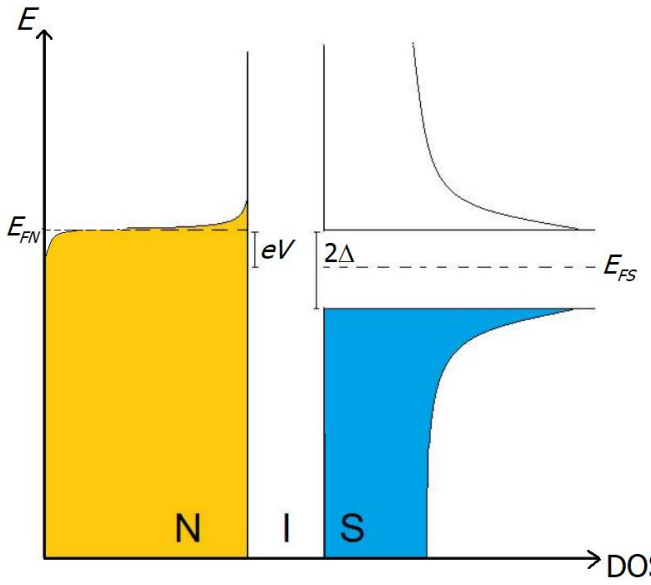

Figure 11. A semiconductor model density of states of a normal metal-insulator-superconductor (NIS) junction at $0 < T < T_c$. The occupied states are coloured. E_{FN} is the Fermi level of the normal metal, E_{FS} is the Fermi level of the superconductor, Δ is the superconducting energy gap, and eV is the energy difference of the Fermi levels, where V is the voltage difference created by a bias. For the currents, $I_N = I_S$.

2.3.4 SINIS-junction

A Josephson junction is a junction between two superconductors connected by a weak link, across which Cooper pairs can tunnel. A weak link can be a normal metal layer, a constriction in a superconductor, or as in this study, an insulating oxide layer [73]. In superconductor based tunnel junctions, Josephson effect is generally dominant at low bias currents and temperatures, whereas at high bias currents and temperatures quasiparticle tunnelling is the dominant method of tunnelling [68]. The SINIS tunnel junctions associated with this work do not exhibit Cooper pair tunnelling, because the tunnel barrier prevents the leakage of supercurrent from the normal metal, as Andreev reflection is prevented by the barrier. For the SNS heater there are no barriers, but the relatively large size of the normal metal island, which far exceeds the coherence length for Al, prevents supercurrent from flowing across the normal metal island. [73]

The so called semiconductor model of a NIS-junction is illustrated in Figure 11. When $T > 0$, there is a nonzero probability of a particle tunnelling across a potential

barrier, represented in the figure by I. In the presence of a bias voltage eV, the Fermi level of a normal metal is altered. If the level is raised, and $eV > \Delta$, the electrons from the normal metal can tunnel into to the superconductor even at $T = 0$ [73]. At $T > 0$, even with $eV < \Delta$, some thermally excited electrons are able to tunnel through the barrier, creating a finite current in the subgap region. With a constant current bias, this voltage becomes dependent on the temperature, making the junction applicable to thermometry.

The current-voltage behaviour of a NIS-junction is given by the equation [68]

$$I(V) = \frac{1}{2eR_T} \int_{-\infty}^{\infty} N_S(E)[f_N(E - eV) - f_N(E + eV)]dE, \tag{78}$$

where V is the voltage bias over the junction, e is the elementary charge, R_T is the tunnelling resistance, $f_N(E)$ is the Fermi function of the normal metal in a quasiequilibrium, E is the energy, and $N_S(E)$ is the quasiparticle density of states [68]

$$N_S(E) = \left| \mathrm{Re}\left[\frac{E + i\Gamma}{\sqrt{(E + i\Gamma)^2 - \Delta^2}} \right] \right|. \tag{79}$$

Γ is a constant called the Dynes parameter. The Dynes parameter is essentially a parameter modelling the pair-breaking rate [68], or inelastic quasiparticle scattering, within the superconductor. However, a similar theory can be also used for the modelling of photon assisted tunnelling, and the Dynes parameter can therefore be used in the fitting of the leakage current in the subgap region essentially as a measure of nonideality [18].

2.3.5 Effects of geometry and materials

The superconducting part of the junction is generally aluminium due to the ease of growing aluminium oxide (AlO_x) barriers of good quality on top of an aluminium film. The normal metal material that has been more widely used, at least in our research group, has been copper. However, more recently a titanium-gold bilayer, with the Ti layer being 5 nm and Au layer being $\geq$ 20 nm has been found to be promising [78]. The advantages of Ti-Au compared to Cu as a normal metal include greater durability, both in terms of chemical attacks during the fabrication and a smaller risk of breakdown due to static charges. The resilience to static charges is caused by a lower specific tunnelling resistance. The Ti-Au devices also exhibit a

stronger cooling power compared to a Cu device [78].

Recent thermal conductance measurements for PnCs in our research group have been conducted with both the heater and the thermometer being a SINIS-junction, fabricated "face-to-face" [18, 21]. However, there are some factors in this geometry which complicate the interpretation of the measured data. In the first place, only a certain percentage of the heat emitted by the heater is intercepted by the thermometer. Calculating this so-called view factor complicates the data analysis. Another factor considering the emitted heat is that because the SINIS-heater island resistance includes tunnel junctions with obviously larger resistance than the normal metal, practically all of the heat is generated by the tunnel processes, half of which is dissipated in the superconducting lead.

To combat these issues, a new measurement geometry was recently developed in the group [37]. In this design, the heater is an SNS device encircling the SINIS-thermometer, pushing the view factor close to unity. A scanning electron microscope image of an SNS-SINIS pair with this geometry is shown in Figure 12. Because of the absence of tunnel junctions, the heat is emitted evenly from the normal metal part. The normal metal part consists of a Ti-Au bilayer, and the superconducting leads in the heater are niobium. Niobium has the highest critical temperature and the largest gap of elemental superconductors (9.25 K) [28], and therefore also a high critical current and thermal isolation properties. This combined with the absence of a tunnelling barrier allows for a large range for the heating experiment.

As a downside to this geometry, the fabrication of the SNS-SINIS pair is somewhat more challenging compared to the design with two SINIS-junctions. For the old geometry, the patterning and the metal evaporation of both junctions could be done simultaneously. For the new geometry the SNS and the SINIS need to be fabricated separately, which increases the number of fabrication steps and thus fabrication time. The increasing of steps also necessarily increases the probability of something going wrong during the fabrication.

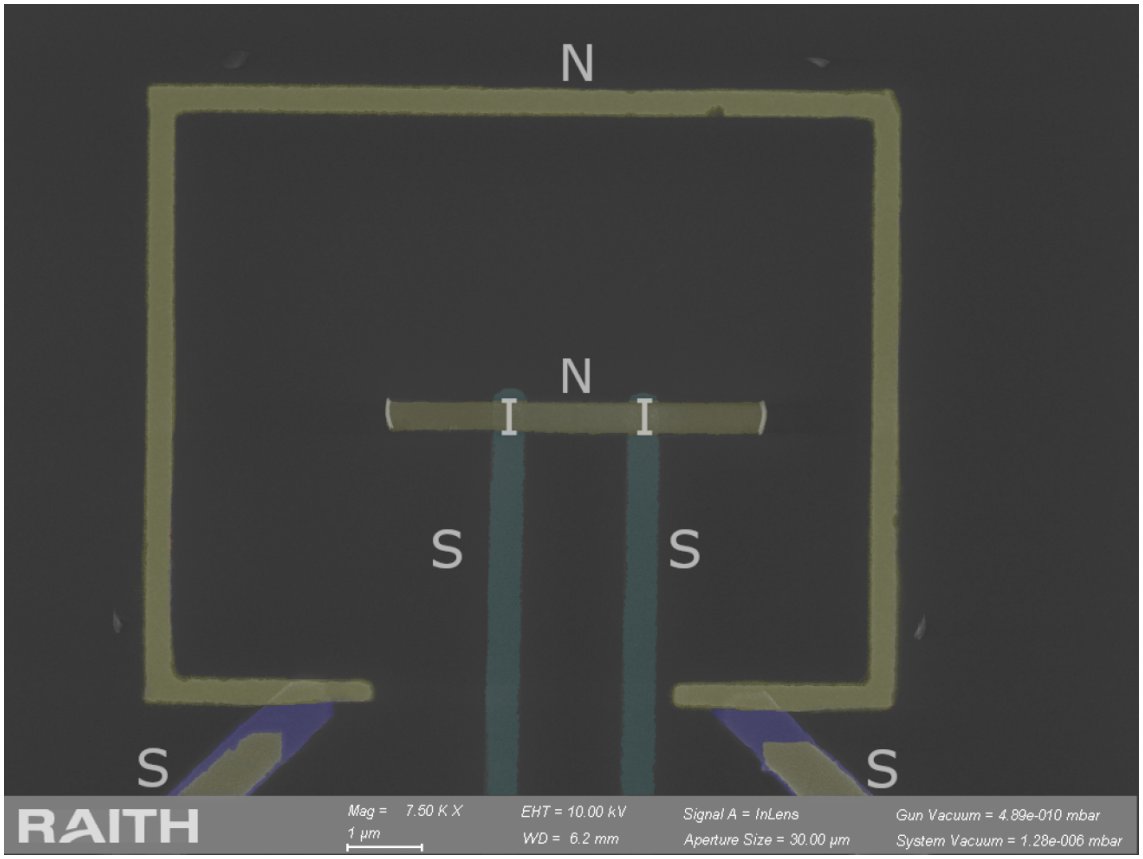

Figure 12. A SEM image a SNS-SINIS-heater-thermometer. The image is coloured to highlight the different metals. Gold is coloured as gold, turquoise or lighter blue is aluminium and dark blue is niobium. S means superconductor, N is normal metal and I is insulator. Note that there is superconducting Nb beneath the Au layer in the wires leading to the normal metal.

3 Fabrication

The sample fabrication was done in the Nanoscience Center cleanroom. The samples were fabricated on approximately 7×7 mm chips cut from a commercial single crystalline $\langle 100 \rangle$ lattice direction silicon wafer with 300 nm of silicon nitride (SiN) on each side. The fabrication process could be divided into four distinct steps: fabrication of the suspended SiN films, the phononic crystal structure, the SNS heater and the SINIS thermometer. The fabrication steps along with the most important processes are presented in Table 1. Figure 13 gives a pictorial representation of the fabrication steps.

Table 1. Fabrication steps.

Fabrication step	**Process**	**Equipment**
1. Suspended SiN film	Chip cleaning	Sonicator
	Resist application	Spin coater
	E-beam lithography	SEM
	Reactive ion etching	RIE
	KOH-etching	Wet-etch bench
2. PnC pillars	Resist application	Spin coater
	E-beam lithography	SEM
	O2 plasma cleaning	RIE
	Al evaporation	UHV evaporator
3. SNS-heater	Resist application	Spin coater
	E-beam lithography	SEM
	O2 plasma cleaning	RIE
	Ti + Nb + Au evaporation	UHV evaporator
4. SINIS-thermometer	Resist application	Spin coater
	E-beam lithography	SEM
	O2 plasma cleaning	RIE
	Al evaporation	UHV evaporator
	Oxidation	UHV evaporator
	Ti + Au evaporation	UHV evaporator

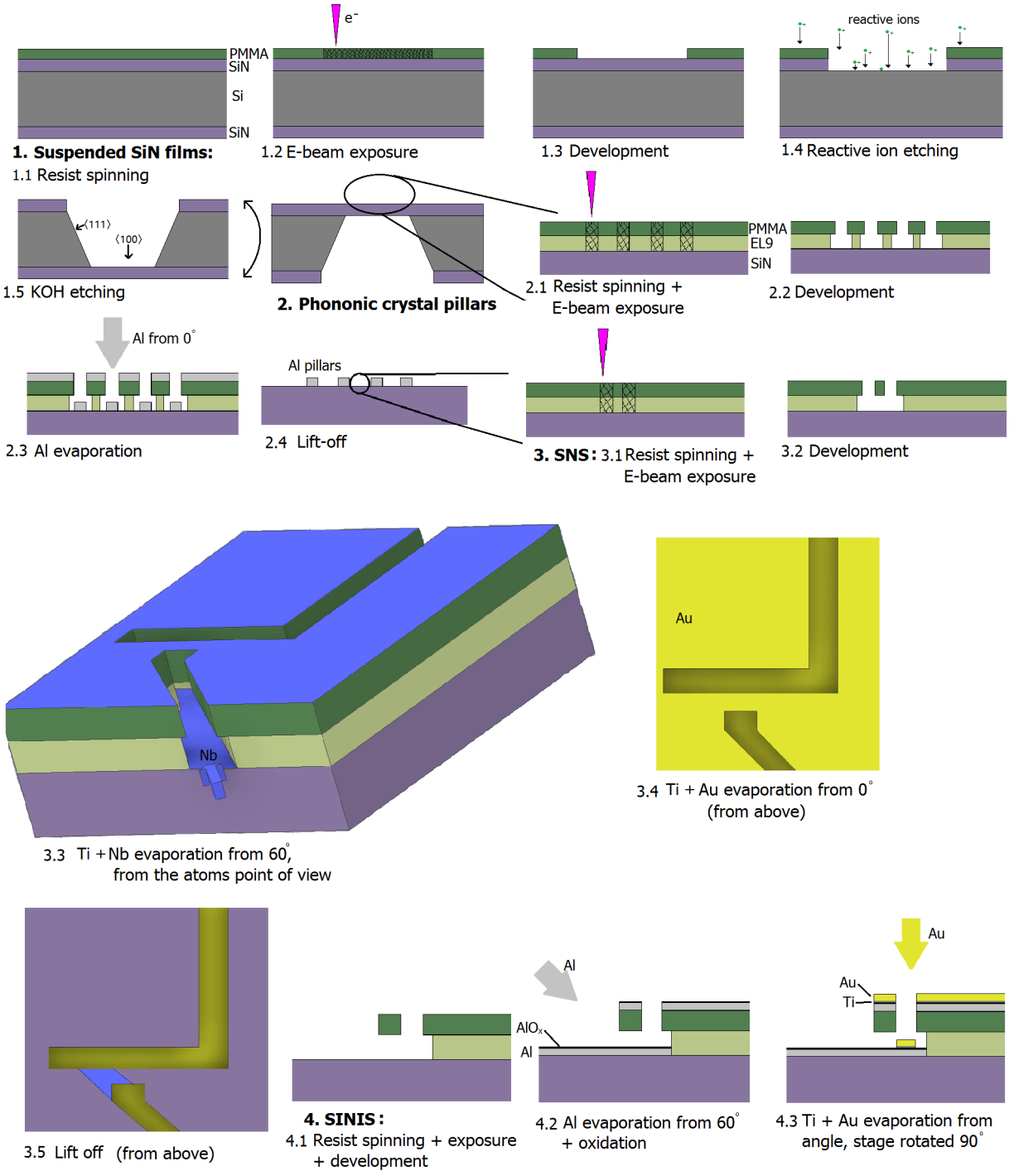

Figure 13. Sample fabrication steps. The 3D images were drawn with ACAD Inventor.

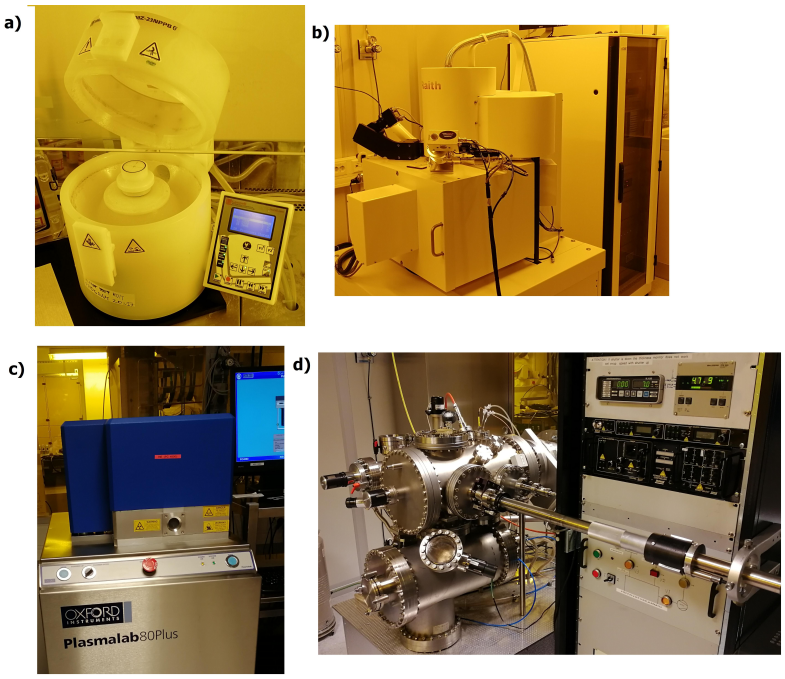

Figure 14. The most essential equipment used for sample fabrication: a) the spin coater, b) eLine scanning electron microscope, c) the reactive ion etcher (RIE), and d) the UHV evaporator.

3.1 Suspended SiN films

After the chips were cut from the wafer they were cleaned. This was done by sonicating them in warm acetone for 5 minutes with a FinnSonic M3 ultrasonicator, after which the chips were wiped with a cotton swap and rinsed with clean acetone and isopropanol (IPA). The chips were dried with a nitrogen gas gun.

The cleaned chip was then coated with a 7 % solution of 950 polymethyl methacrylate (PMMA) in anisole, abbreviated to 950 PMMA A7. The spin coating was done with a Laurell WS 650 Spin Coater at 3500 rpm for 1 min, resulting in a layer of approximately 750 nm of PMMA. The chip was baked for 2 min in 160 °C afterwards to remove the solvent from the PMMA layer.

To create the suspended films of desired size, the PMMA coating was patterned using electron beam lithography (EBL). PMMA is a positive e-beam resist, so exposure to an electron beam with a certain energy breaks the bonds of the polymer chains, making the exposed areas more soluble. The EBL was done with Raith eLine scanning electron microscope (SEM). For the patterning, a 20 kV electron beam

was used with a 120 μm aperture, a 215 $\mu C/cm^2$ area dose and a 1000 μm write field. Because the resolution was not of high priority in this process step, the largest aperture and a high current mode were used resulting in a current of approximately 10 nA and a short exposure time of $\sim$ 10 minutes for one chip.

After the exposure the pattern was developed following a standard procedure of submerging the sample for 40 s in a 2:1 solution of IPA and isobutyle ketone (MIBK). The reaction was stopped by washing the sample with IPA for 1 min and drying the chip with the nitrogen gun.

A Reactive ion etching (RIE) process was then used to etch through the SiN layer on the exposed back side of the chip. The SiN was etched in Oxford Plasmalab80Plus RIE using a manufacturer given room temperature recipe for SiN: 100 W RF power, 30 °C, 55.0 mTorr pressure and 55.0 sccm total gas flow. The reaction gas was a 10:1 mixture of CHF_3 and O_2. The exact thickness of the SiN layer was actually unknown due to poor documentation, even though the thickness was presumed to be 300 nm. The thickness could still be defined with a decent accuracy. The etching rate of the used RIE recipe is 30.9 $\pm$ 0.7 nm/min [35]. Because 10 minutes of etching was not sufficient to etch through the SiN layer, but a 11 min process was, it is reasonable to assume that the SiN film thickness on the wafer is between 300 nm and 345 nm. Also, a measurement with Rudolph AUTO EL III ellipsometer gave a thickness of 320 nm.

After the RIE step, the chip was wet etched at 97 °C in a 34 % solution of potassium hydroxide (KOH) for approximately three hours. KOH does not react with SiN, and etches silicon in the direction of the $\langle 111 \rangle$ lattice plane very slowly, which results in a 54.74 ° sidewall angles etch in the $\langle 100 \rangle$ direction [79]. This allows for an anisotropic etch for creating rectangular suspended SiN films. The windows created in the film with EBL and RIE were 680 $\times$ 680 nm squares, which resulted in $\sim$ 300 $\times$ 300 nm SiN films on the front side of the chip. After the chip was removed from the KOH it was first rinsed in deionised (DI) water, after which it was cleaned in 0.09 % HNO_3 solution for 3 minutes and rinsed in DI water and IPA. The nitric acid cleaning was performed because the chip frequently cam out looking dirty from the KOH, and there were some crystals of unknown material on top of the film visible with a microscope. Even this brief washing in the dilute HNO_3 solution was able to almost completely eradicate this problem.

3.2 Fabrication of the phononic crystal

For the pillar fabrication, the chip was initially coated with a PMMA copolymer P((8.5)MAA)MMA in a 9 % ethyl lactate solution, abbreviated to EL9. Two layers at 3000 rpm were spun on the chip, each layer being baked for 1 minute at 160 °C. The result was a ∼750 nm thick layer of EL9. The purpose of the copolymer was to ease the lift-off process by preventing any excess metal on the resist from evaporation from sticking to the pillars, which would interfere with the lift-off. On top of the EL9, two layers of 950 PMMA A4 were spun at 3500 rpm creating a combined layer thickness of ∼ 400 nm. Each PMMA A4 layer was baked for 2-3 minutes at 160 °C. Between the PMMA layers a 5 mn layer of aluminium was evaporated using a physical vapor deposition (PVD) process with the Ultra high vacuum electron gun evaporator (UHV evaporator) located in the cleanroom. The purpose of the aluminium layer was to prevent charging of the insulating layers of PMMA and SiN during the EBL, allowing electrons to propagate in the material. It was discovered that if the aluminium layer was not present, the pillar rows would be misaligned due to the electron beam being deflected by accumulated electrons in the PMMA and the SiN.

The acceleration voltage and the area dose for the EBL were again 20 kV and 215 $\mu C/cm^2$. A smaller aperture of 30 μm and a current of approximately 0.3 nA were used for a finer resolution. The area of the pillar structure was 200 × 200 μm, so a 200 μm write field was used to expose the whole crystal pattern with a single write field. This prevented even the slightest misalignment. Along with the crystal pattern two sets of markers, three large and three smaller ones, were also drawn to facilitate the the alignment in the later process steps. The EBL design for the entire device, including the bonding pads, is shown in Figure 15. Two different periodicities, 5 μm and 1 μm , for the pillar structures were fabricated, both with a filling factor of 0.6 in the design, translating to 0.65 filling factor in the finished sample.

After the exposure the development was done according to the following steps: 15 s submersion into 2:1 IPA MIBK solution (developer 1), 1 min cleaning with IPA, 10 s submersion into room temperature KOH solution to remove the 5 nm of aluminium, washing with DI water and IPA, a second 15 s development in developer 1 to remove the PMMA below the Al, a 5 s exposure to 2:1 solution of methanol and methoxyethanol (developer 2) to develop the copolymer and to create an undercut.

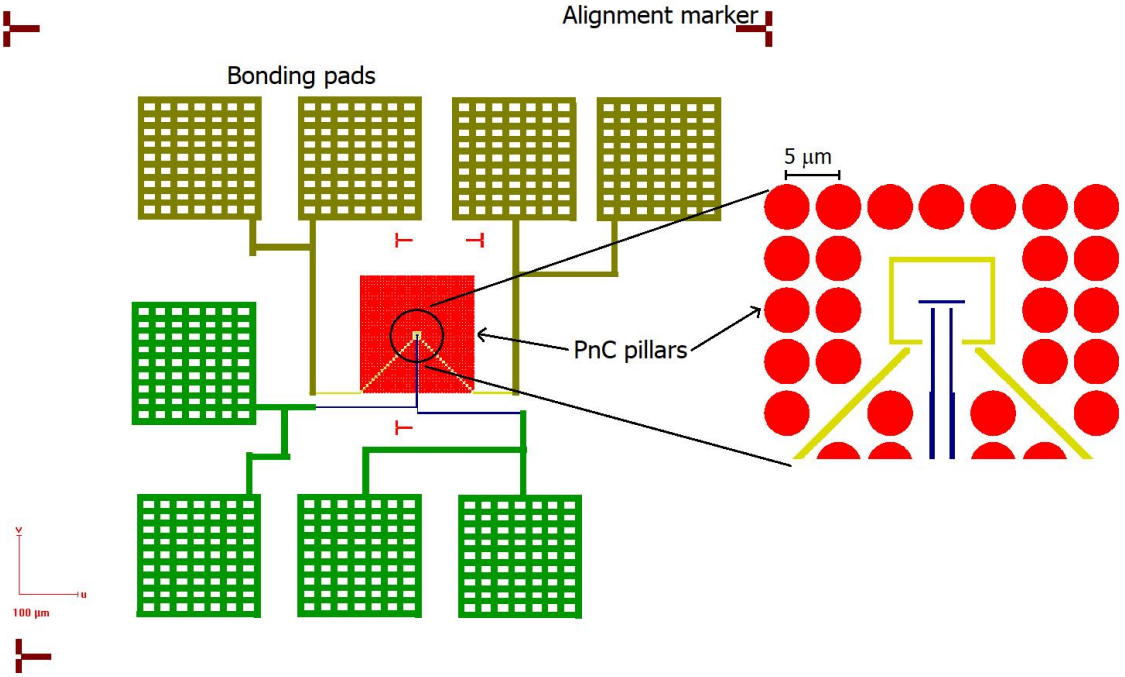

Figure 15. Design for the electron beam lithography including a zoom-in on the area around the heater-thermometer, drawn with the Raith program. Different layers are represented by different colours.

Finally the reaction was stopped by a 1 min submersion in IPA, and the chip was dried with the nitrogen gun. After the development, the chip was examined under an Olympus BX51M optical microscope. If the pattern was not a desired one, the fabrication step was repeated from the beginning.

The metal pillars were deposited using the UHV evaporator. Before the evaporation, any excess residues of the resist from the developed areas were removed using an O_2 cleaning process with the RIE with 60 W RF power, 40.0 mTorr pressure and 50.0 sccm gas flow with a 45-60 s process time. For aluminium pillars the evaporation rate was 0.1 nm/s, and the calibration factor was determined with the Bruker Multimode 8 atomic force microscope (AFM) to be 1.25. With this calibration evaporating a 300 nm layer of aluminium from a 0 degree angle the evaporation thickness monitor reading was 240 nm. The pressure inside of the evaporation chamber was generally in the range of 10^{-9} and 10^{-7} mbar, depending on the evaporated metal, the current frequency of use of the device, and when the vacuum chamber was last opened.

The lift-off, or the removal of the metal in the areas that were not patterned, was done by immersing the chip in acetone near its boiling point. The hot acetone

was also sprayed onto the chip with a syringe until the metal layer appeared to be removed. The results were then investigated under the optical microscope, and the lift-off process was repeated if there was any unwanted metal remaining.

In the fabrication of the 1 μm period PnC sample the copolymer was omitted from the pillar fabrication step, and 3 layers of PMMA A4 deposited with 2500 rpm were used instead. The resulting layer was approximately 600 nm thick, and the 5 nm Al layer was evaporated between the second and the third layer. The reason for this was that after developing the copolymer the PMMA A4 layer collapsed with lack of any support, which prevented the lift-off. For the 5 μm pillars, some copolymer remained to support the PMMA layer, which prevented such a collapse. As the lift-off was successful without a copolymer, it is probable that no EL9 layer would have been required with the 5 μm pillars either.

3.3 SNS and SINIS fabrication

The fabrication of the SNS heater and the SINIS thermometer was done in two different lithography cycles, but the steps were fairly similar. In both the SNS and the SINIS fabrication the resists applied were EL9 at 2500 rpm (∼350 nm) baked for 1 minute at 160 °C, and two layers of 950 PMMA A4 at 2000 rpm (∼700 nm combined) baked for 2-3 minutes at 160 °C. A 5 nm aluminium layer was once again evaporated between the layers of PMMA. As even the first resist layer was thicker than the height of the pillars, there appeared to be no problems with the spinning of the resist.

The acceleration voltage for EBL for both the SINIS and the SNS was again 20 kV. The are dose was 300 $\mu C/cm^2$ for all structures. For the smaller parts of the pattern the 30 μm aperture was used with a 50 μm write field to achieve the necessary resolution. As the write field was not big enough to fit all of the thinner lines with the junctions, the write field had to be manually aligned with the software's write field alignment procedure. To further increase the resolution and to confirm the alignment of the write field a beam spot was exposed in the vicinity of the are to be patterned, and the final focusing, the stigmation correction and the write field alignment were done on the spot. The larger parts of the leads and bonding pads (Figure 15) were exposed with a 120 μm aperture, a current of ∼5 nA and a 1000 μm write field.

To create the pattern precisely in the right spot in the empty space space inside the pillar array, a 3-point alignment procedure provided by the software was utilised. First, one of the larger alignment markers created along with the pillars was located. An angle correction was performed with the two large markers above the design. Then the coordinate system of the software was set to match the location of one of the markers. After this rough alignment was made, the smaller markers closer to the centre of the structure were located (see Figure 15), and an angle correction was again performed on the two markers with the same y-coordinate. Then the 3-point alignment procedure was performed, where each of the real marker locations was set to match the marker location in the design. This way the location of the exposure could be set very accurately.

The development steps for the SINIS and the SNS both were 20 s in developer 1, 1 min clean with IPA, 10 s in room temperature KOH, washing with DI water and IPA, 20 s in developer 1, 7 s in developer 2, and 1 min in IPA. The parameters for the O_2 clean were the same as the cleaning done for the evaporation of the crystal structure.

For the SNS heater the superconducting leads leading to the titanium-gold normal metal were of niobium with a thin layer of titanium underneath. A 5 mn layer of Ti was evaporated from a 60 ° angle (Figure 13) from the sample normal with evaporation rate of 0.1 nm/s. Then a 20 nm layer of Nb was evaporated from the same angle at 0.2 nm/s. The purpose of the Ti layer here was to create a barrier between the Nb and the SiN in the film, as the Nb layer will grow to be of higher quality in the presence of the Ti barrier [80]. The larger evaporation rate of Nb was to decrease the grain size to reduce oxygen pathways that would lead to a deeper oxidation and a lower quality film [80, 81]. Then the sample stage was rotated 90 ° in the xy-direction, and the same thicknesses of Ti and Nb layers were evaporated to form the second superconducting lead. Then another 5 nm of Ti was deposited from 0 °. The purpose of this Ti layer was to work as an adhesive for the gold. A 20 nm layer of Au was then evaporated from 0 ° on top of the titanium. This created the normal metal link between the superconducting leads. The lift-off procedure was similar to that of the pillar fabrication phase. The width of the Nb leads near the heater were 1 µm , and the Ti-Au wire was 300 nm wide.

Several times during the thesis project it was discovered that the after the evaporation

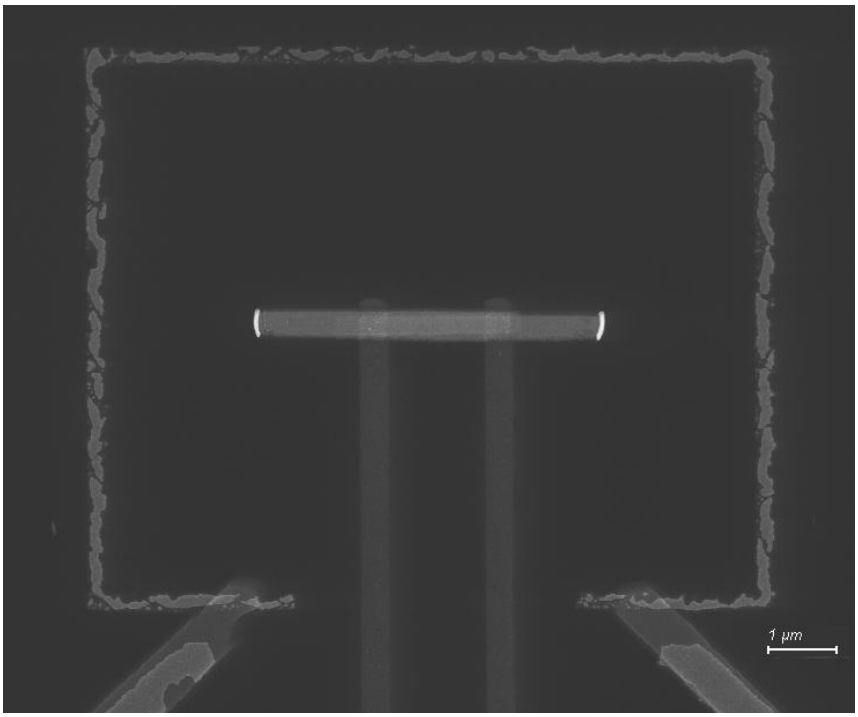

Figure 16. A SEM image of the heater-thermometer fabricated with an aged EL9 copolymer. The normal metal part of the SNS-junction is notably thinner than it should and not intact.

and the lift-off, the normal metal part of the SNS-junction was not fully intact. When this was the case, often times the normal metal Au would only show faintly in the optical microscope images or not at all. Sometimes there were parts that were clearly missing, or the Au wire consisted of small "islands". An image of an example of this problem is shown in Figure 16. This was also occasionally observed with the Al wires leading to the SINIS junction. Fortunately, this problem had also previously been encountered during the fabrication in [37]. Apparently the copolymer EL9 had aged, as producing a new solution from the EL11 stock solution seemed to immediately fix the issue for a while, although the problem usually appeared again in a few weeks. After this had been going on for a while, a new bottle of ethyl lactate was produced. A solution made from this new bottle appeared to age more slowly, as the first solution made from the new bottle persisted through the rest of the fabrication work. Fro addition the SNS normal metal part and the SINIS superconducting wires were made slightly wider as an attempt to improve the yield of the overall process. The SINIS wires were not widened around the tunnel junction to keep the junction area constant.

After confirming the wires in the SNS structure were intact, a similar lithography process as described for the SNS structure was conducted, this time to create the SINIS-junction. The alignment was done for the same markers created during the PnC fabrication phase, and similar apertures and write fields were used for the smaller and the larger structures. The metal deposition began by evaporating 20 nm of Al from 60 ° angle with the familiar rate of 0.1 nm/s (Figure 13). This created the superconducting wires leading to the junction. Next the insulating barrier of AlO_x was created by transferring the sample to the loading chamber of the UHV evaporator, and exposing it to a 200 mbar of pure oxygen atmosphere for 5 minutes. The sample stage was then rotated 90 degrees, and the stage was pulled back into the evaporation chamber. Ti was once again used as an adhesive for the Au normal metal. To have an even layer of the normal metal evaporation was done in several angles. First Ti and then Au were evaporated from both sides from 55 °, 50 ° and 45 ° angles, at a rate of 0.1 nm/s. 0.7 nm of Ti was deposited per turn, making the final Ti thickness 4.2 nm. The final Au layer thickness was 21 nm, resulting from evaporating 3.5 nm per turn. The Al leads and the Ti-Au wire were both 300 nm wide.

The lift-off was again done in hot acetone, and the results were first examined under the optical microscope. An image of the finished design is presented in Figure 17. The integrity of the wires and the existence of a tunnel barrier was confirmed by measuring the room temperature resistance of the junctions with a Fluke 175 digital multimeter. The multimeter was attached to micrometer-scale probes that allowed the measurement of resistance from the bonding pads. Typical room temperature resistances for the SNS-junctions were $1.5 - 2.5\mathrm{k}\,\Omega$, and typical SINIS resistances were $4 - 7\,\mathrm{k}\Omega$. If the resistance of the SINIS was equal or below the resistance of the SNS, it was assumed that no tunnelling barriers were present.

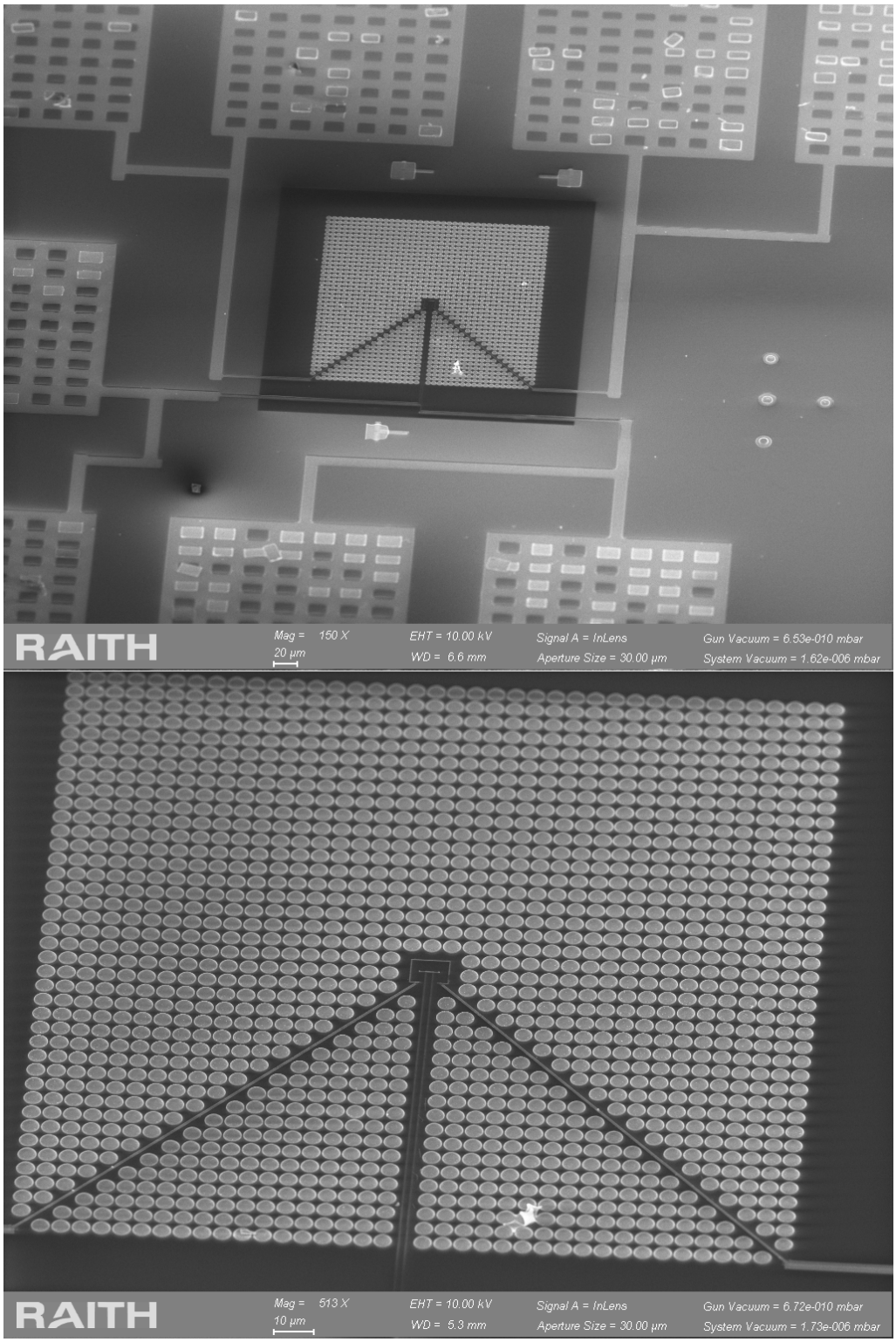

Figure 17. SEM images of the finished phononic crystal device with the heater-thermometer, taken from a 45 ° angle. The suspended area of the SiN film can be seen as the darker square in the upper image.

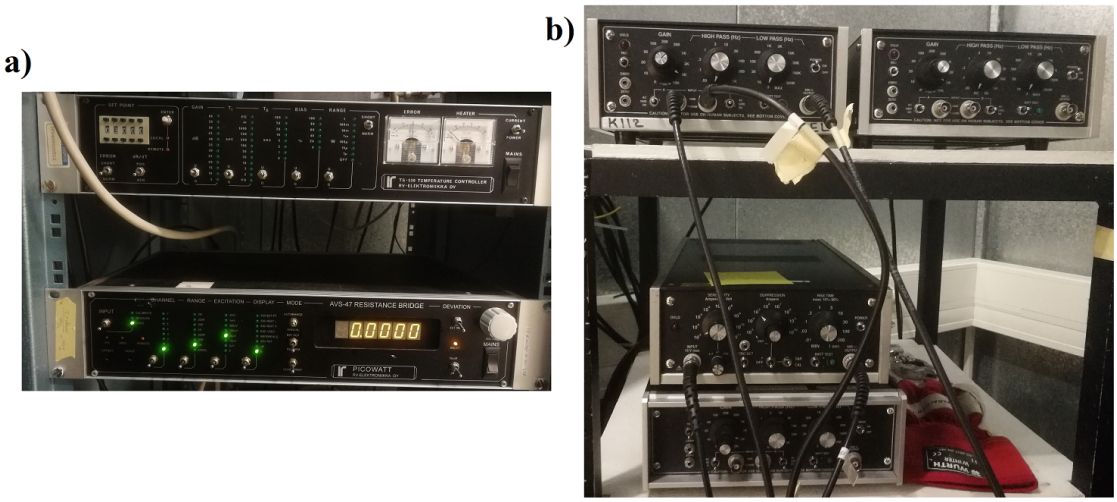

Figure 18. Some of the most crucial electronics used in the measurements: a) The PID-controller on the top, and the resistance bridge on the bottom. b) The voltage amplifiers and the current amplifier.

4 Methods

4.1 Measurement equipment

The measurements were conducted in an electrically shielded measurement room in the Nanoscience Center. The room functioned as a Faraday cage which would shield everything inside from external electromagnetic radiation. The room also had a ground separate from the standard building ground to prevent any noise or current spikes originating from other devices.

An analogue voltage sweep box was used as the voltage source for the measurements. The sweep box was powered by a car battery to prevent noise from the electrical grid. The voltage signals were amplified with two DL Instruments 1201 voltage amplifiers, and the current was amplified with a DL Instruments 1211 current amplifier (Figure 18). The analogue signals from the amplifiers were fed to a National Instruments BNC-2090 Data Acquisition System, and the signal was converted to a digital form with a National Instruments PXI-6251 ADC. The digital signal was then sent to a

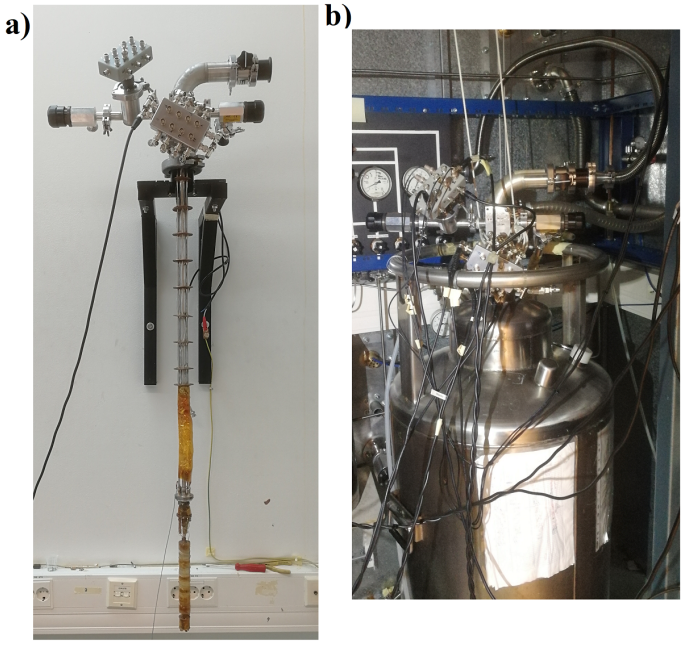

Figure 19. a) The bare PDR dilution refrigerator "Noiseless". b) The cryostat in a He dewar during a measurement.

computer via an optical fiber. A home-made battery powered current source was used for a source for a constant current.

The electrical measurements were done below 1 Kelvin. The cooling to these temperatures was achieved with a home-made ^{3}He/^{4}He dilution refrigerator "Noiseless" (Figure 19), which was able to reach temperatures around 50 mK. The cryostat contained a RuO resistance thermometer, which allowed for a precise monitoring of the sample stage temperature at low temperatures. The thermometer resistance was read with an RV-Elektroniikka Picowatt AV47 resistance bridge, and the signal was transferred to a computer via the same route as with the amplifier signals. The temperature of the stage could be fixed with a <1 mK accuracy with an RV-Elektroniikka TS-530 PID (proportional-integral-derivative) controller, which was connected to a heater in the sample stage.

Multiple stages of electrical filters were present at different temperatures along the measurement lines. At the base of the cryostat sample stage, integrated into the stage bonding pads, were simple RC low-pass filters. At the base temperature level there were also meander-line high-frequency metal powder filters. The purpose of these filters was essentially to filter out any thermal noise. At 1 K a metal powder

feedthrough was used for additional filtering. At liquid He temperature, 4 K, the lines had commercial pi-filters. Additionally, the amplifiers used also possessed their own output filters, set for low-pass/DC for the measurements.

The working principle of a ^{3}He/^{4}He dilution refrigerator is based on the phase behaviour of a ^{3}He and ^{4}He mixture at sub-Kelvin temperatures. Below a certain temperature the mixture undergoes a separation into two phases, one with a high concentration of ^{3}He and one with a low concentration of ^{3}He, referred to as the concentrated and the dilute phase, respectively. The dilute phase has a larger enthalpy than the concentrated phase, so transferring ^{3}He atoms to the dilute phase requires energy, which is taken as heat from the environment. This is the source of the main cooling power of the device. The ^{3}He is moved from one phase to another by pumping it through a circulatory system involving multiple heat exchangers and a still heater enhancing the circulation. Although the initial gas mixture has a proportion of approximately 30 % of ^{3}He, the circulating gas is almost entirely ^{3}He due to it having a higher vapour pressure, the ^{4}He being condensed in the mixing chamber.

The phase separation temperature is below 1 K, and is dependent on the concentration of the initial mixture. This temperature is reached by first cooling down to 4 K with liquid helium-4, after which a temperature of ~ 1. K is achieved with a pot cooler, where the cooling is created by pumping of ^{4}He from the dewar. Both components of the mixture liquefy at this temperature. Then the condensed mixture is pumped until the phase separation temperature is achieved, in the case of our system around 0.7 K.

4.2 Measurements

To determine the thermal conductance reduction of the phononic crystal, the emitted phonon power as a function of temperature of an unaltered 300×300 μm 300 nm thick SiN membrane and a similar membrane with two pillar-based phononic crystal with Al pillars of $h = 300$ nm, a filling factor of 0.65, and periods of $a = 5$ μm and $a = 1$ μm were measured. These results were then compared with each other and with the coherent theory simulation data. The measurement procedure and the data analysis were identical for all samples. In this chapter the measurement of the unaltered membrane is used as an example.

4.2.1 Cooldown

The sample chip was attached to the sample stage of the cryostat with low temperature varnish. A piece of tobacco paper soaked in varnish was placed between the chip and the varnish to allow for air to escape from the cavities below the membranes and to prevent the varnish from making direct thermal contact with the film, without compromising the thermal contact with the chip itself. A Kulicke & Soffa 4523A wire bonder was used to connect the sample bonding pads to the sample stage contacts with Al wires. After the bonding the stage was attached to the cryostat, the connections and the integrity of the device were checked with a multimeter. Then the vacuum jacket and all of the lines of the cryostat were pumped to a vacuum. During all of this the sample stage contacts were connected to the measurement room ground.

After starting up the pumps and checking that no leaks were present, the cooldown was initiated by submerging the cryostat into liquid nitrogen, while a small amount of air was let inside the vacuum jacket to function as a heat exchange gas. Before the submerging the pot was flushed with ^{4}He, and after that kept at a constant pressure slightly above 1 ATM. When the cryostat had reached 77 K, it was quickly transferred into a liquid helium dewar. A small amount of ^{3}He was let into the vacuum jacket to once again function as the heat exchange gas. ^{3}He was used here because it is much easier to pump than ^{4}He, as it remains a gas even at 4 K. The pressurising of the pot was also ceased after this point. Once the vacuum jacket had reached a sufficiently low pressure, the pumping of the pot was initiated, and the cryostat was left to condense the mixture overnight.

If there were no leaks, the cryostat had cooled close to 1 K overnight. A much higher temperature would indicate a leak. With no evident leaks, the circulation of ^{3}He was initiated by beginning to pump the still (dilute phase) side of the circulatory system. The temperature then decreased until reaching the phase separation temperature, where the decrease slowed down, until after a while it greatly accelerated, indicating the phase separation. The cooling was also accelerated by heating the still, which increased the evaporation rate of the ^{3}He. The heating was gradually increased until a temperature close to 50 mK was achieved.

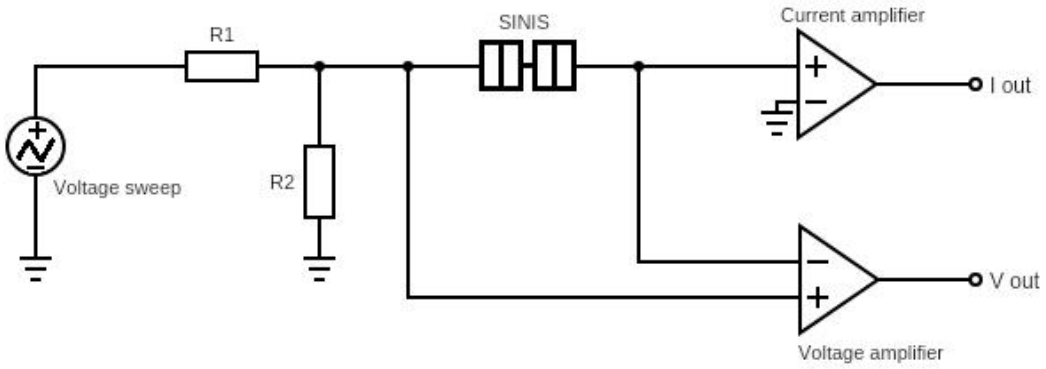

Figure 20. A circuit diagram of the IV-measurements. $R1$ and $R2$ are the resistors for the voltage divider.

4.2.2 IV-measurements

After reaching the lowest achievable temperature of the cryostat, the IV-characteristics of the SINIS-junctions were measured. The measurement circuit was a standard 4-point measurement, a circuit diagram of which is presented in Figure 20. The output voltage of the voltage divider is determined by the resistors R_1 and R_2 by

$$V_{out} = V_{in}\frac{R_2}{R_1 + R_2}. \tag{80}$$

The voltage divider output essentially determined the range of the voltage sweep. Typical divider values during the IV-measurements were 1/1000, 1/2000 and 1/5000. The output signals were amplified and collected through the measurement card. The measurement was run and the data was collected with a LabVIEW-program.

The IV-curves were measured to confirm the existence of a SINIS-junction, and to determine a suitable bias current for utilising the SINIS as a thermometer. For this, the IV-curve was measured at multiple temperatures between 50 mK and 1 K, the temperature having been set with the PID. An example of some IV-curves is presented in Figure 21a. Albeit the amplifiers were manually corrected for offset, there always existed a small offset for both the voltage and the current. This was corrected by taking a numerical derivative of the current data to obtain a differential conductance (dI/dV) curve, for which the voltage offset was corrected by setting the curve to be symmetric around zero bias. The current offset was then corrected

by aligning the zero of the current to the zero of the offset-corrected voltage in the IV-curve. This was done with the Origin software. The amplified values were also converted into physical values by taking into account the gains of the amplifiers. Differential conductance curves derived from the IV-curves are shown in Figure 22.

A suitable bias current was then determined by plotting all of the measured IV-curves on a logarithmic scale. The bias current was chosen so that the voltage would have a maximal change as a function of temperature, to have the optimal sensitivity for the thermometer (Figure 23). BCS-theory fits were done for the SINIS IV-characteristics to obtain the values for the energy gap at zero temperature and the Dynes parameter. A code created by Geng Zhuoran was used for this. Initially the fitting was done using a simple theory, which ignores for instance any heating and cooling caused by the junctions and the normal metal. These fits are presented in Figure 24. As seen from the figure, the simulations do not fit very well. To obtain better fits, a so-called thermal model present in the same code was used. The thermal model takes into account the strength of the electron-phonon coupling and the heating and cooling caused caused by the SINIS-junction, as well as heat flow in the metals. The values for the superconducting energy gap obtained from the fits correspond fairly well to the value of the gap of Al, and the Dynes parameter is in the same order of magnitude as in previous studies within the group [18, 37].

4.2.3 Calibration and the heating experiment

The circuit diagram for the calibration and the heating experiment is presented in Figure 26. The SINIS-thermometer circuit had a floating ground to prevent any current leakage between the two circuits.

The calibration was performed by measuring the SINIS voltage and the stage thermometer resistance while cooling down the cryostat. The cooling down was assumed to be slow enough to have the SINIS junction constantly in a thermal equilibrium with the sample stage. The correct stage temperature was obtained by performing a ninth-order polynomial fit to the RuO thermometer calibration data. This was then plotted with the voltage to obtain the voltage as a function of temperature, shown in Figure 27.

After the calibration, the cryostat temperature was set to a value as low as possible with the PID-heater. This temperature was generally 10-20 mK higher than the

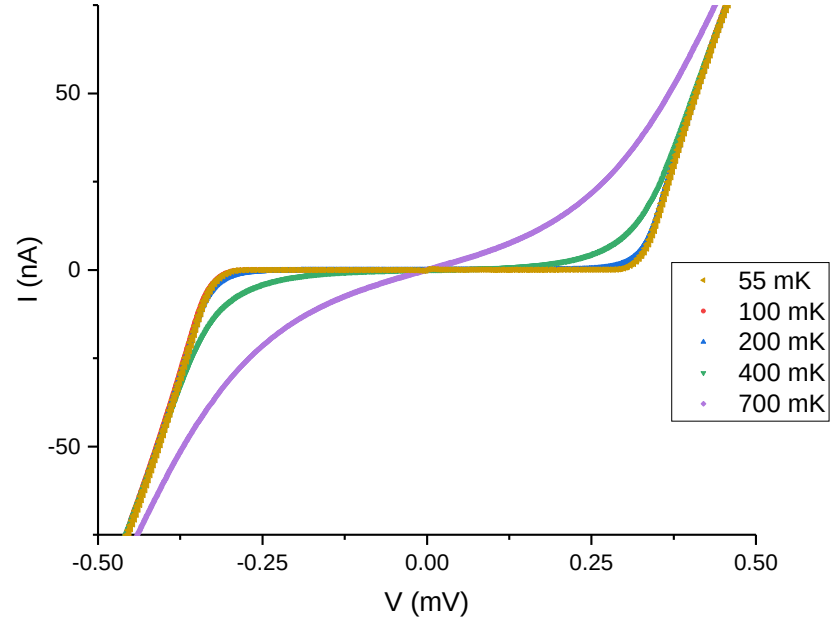

(a) SINIS-IV-curves at different temperatures.

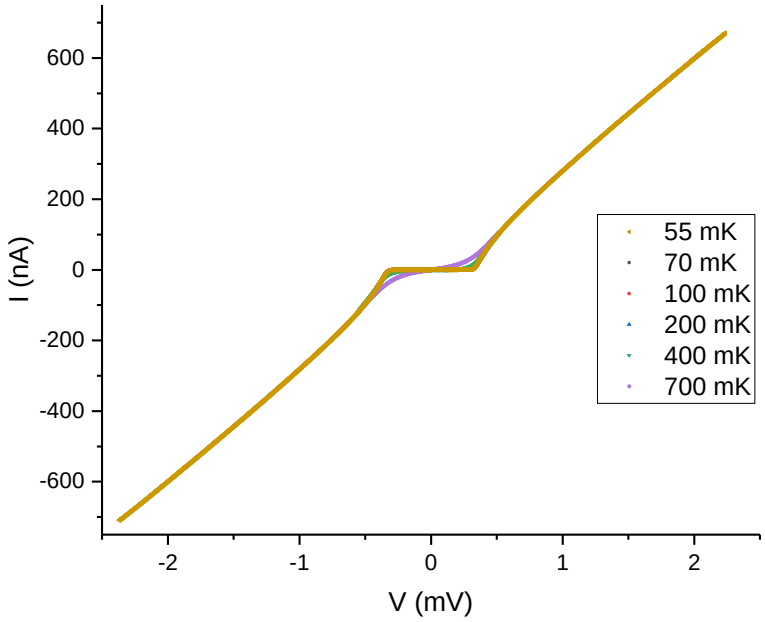

(b) SINIS-IV-curves with the 55 mK curve having a smaller voltage divider.

Figure 21. SINIS-junction IV-curves from the first measurement.

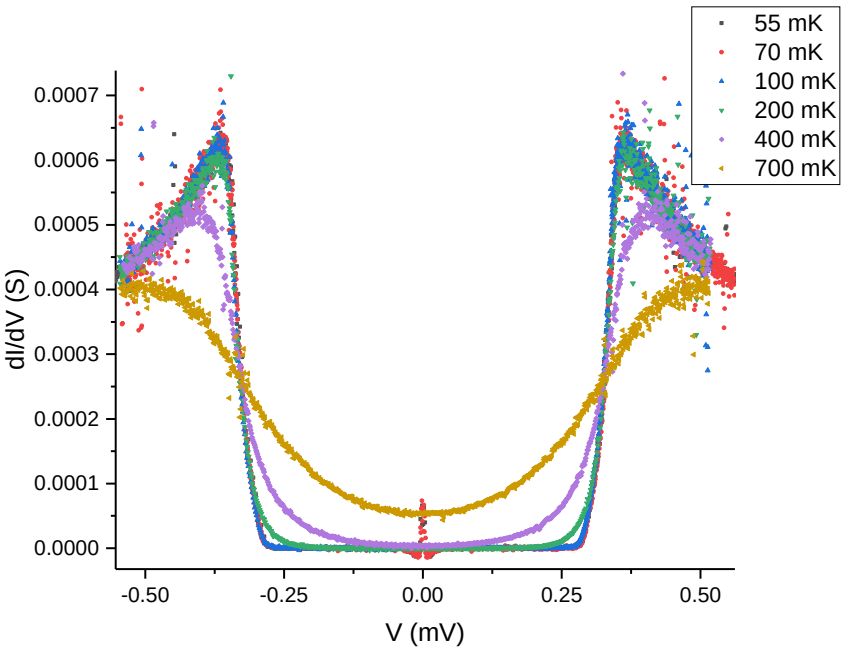

Figure 22. Differential conductance curves of the first measurement for different temperatures. A zero bias peak at $T < 100$ mK can be observed.

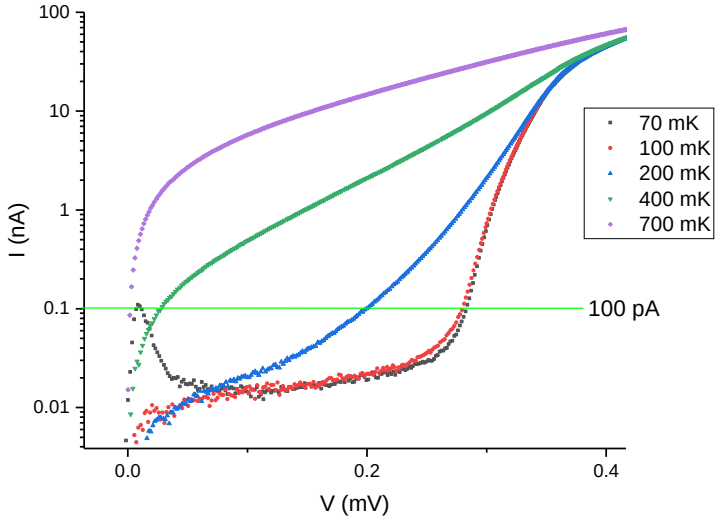

Figure 23. Logarithmic scale IV-curves that were used to determine a suitable bias current. A 100 pA bias current used in the measurements for the unaltered SiN film is shown.

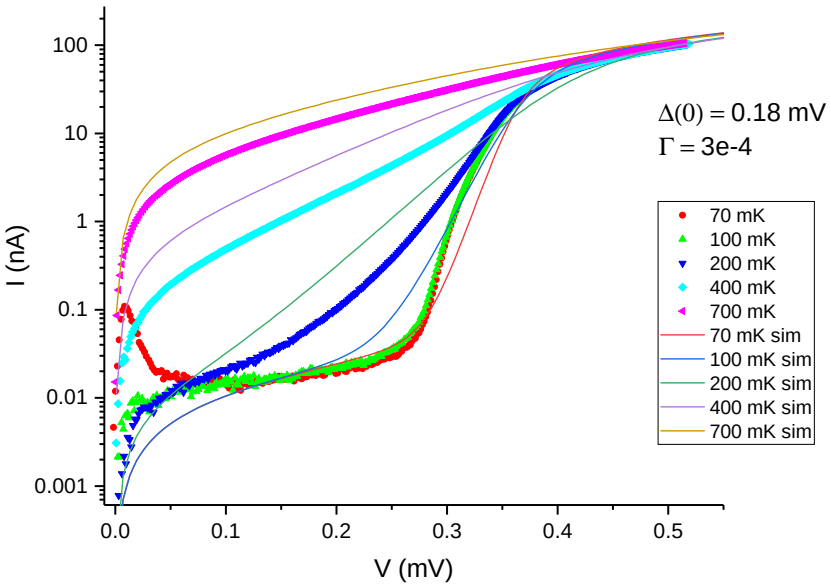

Figure 24. SINIS IV-curves with simulated results based on simple BCS-theory. The energy gap appears to agree with the theoretical energy gap of Al, which is $\Delta(0) = 0.182 \times 10^{-3}$ eV.

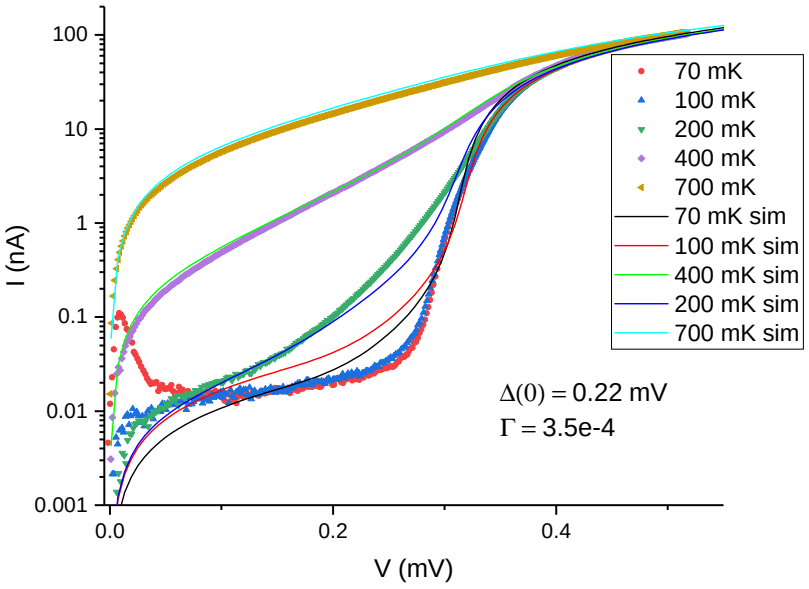

Figure 25. The unaltered membrane IV-curves with thermal model simulations.

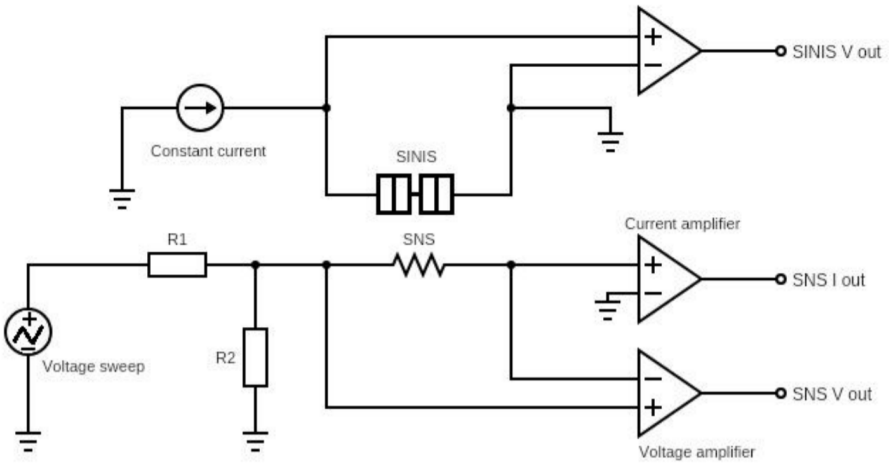

Figure 26. The heating experiment as a circuit diagram. The calibration of the SINIS voltage before the heating experiment was done for the same circuit. The SINIS circuit was floating, so the grounds of the two circuits are not connected.

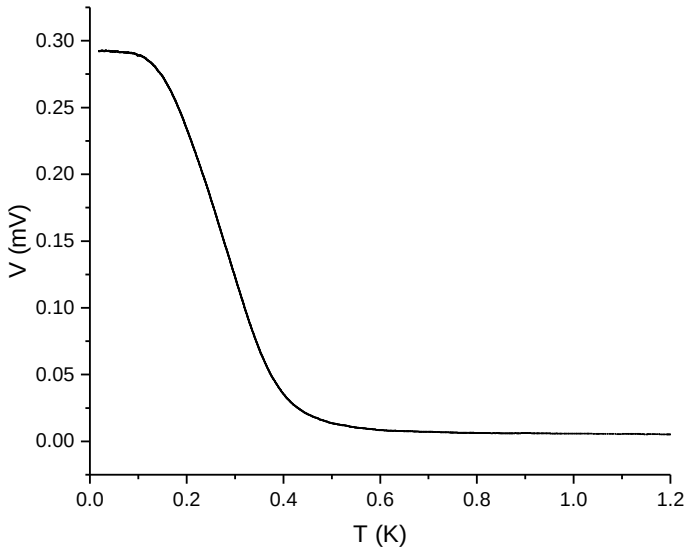

Figure 27. The SINIS calibration curve with a 100 pA current bias used in the measurement of the unaltered film emitted phonon power.

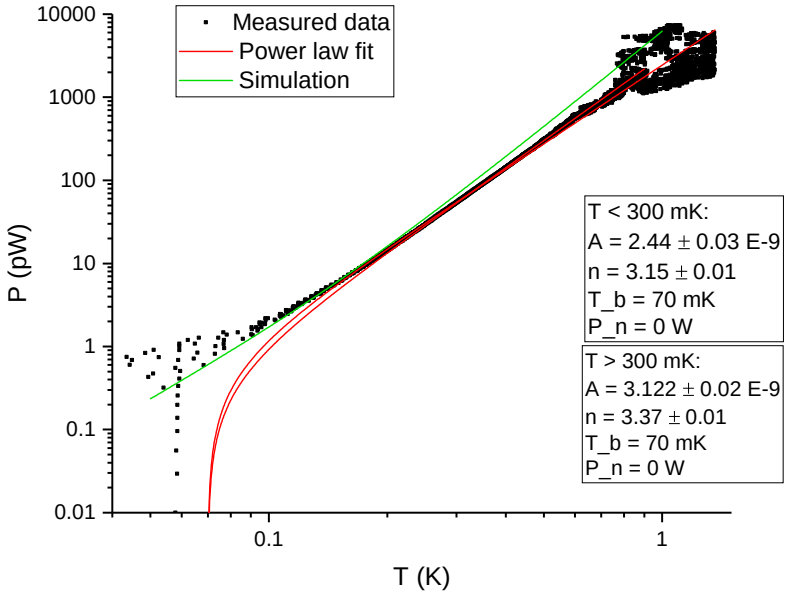

Figure 28. The emitted phonon power measured for an unaltered film. A power law fit divided into two parts is done for the experimental data.

lowest achievable temperature as some heating was required for a stable temperature. This temperature is referred to as the bath temperature T_b. The voltage sweep box functioned as the voltage source for the SNS-heater, and the voltage and current of the SNS and the voltage over the SINIS were measured. Three sets of data with voltage dividers of 1/300, 1/1000 and 1/5000 were measured. An offset correction was once again conducted on the SNS voltage and current. The SINIS voltage was left unaltered, as that would have destroyed the calibration, and absolute voltage values were not required to obtain the temperature from the SINIS voltage.

The temperature of the SINIS was obtained by a linear interpolation of the calibration data, and the power emitted by the heater was calculated from Joule's law $P = VI$. The power was then plotted as a function of the temperature. A simple power law

$$P = A(T^n - T_b^n) - P_{noise} \tag{81}$$

was fitted to the curve, where A, n and P_{noise} are parameters to be determined. The purpose of the P_{noise} term is simply to set the zero of the fit to match the zero of the measured data. Physically, it corresponds to noise heating. The fitting for the

unaltered film data was conducted in two parts, for $T > 300$ mK and $T < 300$ mK, following the example of Ref. [37]. This was done because there was a noticeable change in the power law of the curve, which is expected for a quasi-2D membrane [37, 39]. There is also possibily some effect caused by the self-cooling of the SINIS-junction. The fitting for the unaltered film data is presented in Figure 28. The three resulting emitted power curves from the three measurement runs were compared to confirm they were consistent, and the data used for the fitting and the comparison between different samples was the one with the largest voltage range.

4.3 Simulations

The simulations presented in this thesis are based on fully coherent theory, and were performed by Tuomas Puurtinen. The frequency eigenmodes within the first Brillouin zone for an unaltered film and the phononic crystal were solved using FEM-simulations. The emitted phonon power could then be calculated from the obtained eigenmodes via equation (42).

As the size of the unit cell of the PnC was much larger than the interatomic distance, classical elastic theory was used for solving the eigenmodes within the unit cell from the elastodynamic equations [18]

$$\begin{aligned} -\mu\Delta\mathbf{u} - (\lambda+\mu)\nabla\cdot\mathbf{u} &= \rho\omega^2\mathbf{u} \\ \hat{\mathbf{n}}\cdot\sigma(\mathbf{u}) &= 0, \end{aligned} \tag{82}$$

where $\mathbf{u}$ is a 3D displacement vector, μ and λ are the elastic parameters for the material, ρ is the material density and $\sigma(\mathbf{u})$ is the stress tensor. Experimental values for amorphous bulk materials at room temperature were used. These parameters could differ from the actual values for a thin film at low temperatures, but for a hard material such as SiN the difference should not be great. The second equation is for the assumption of stress free conditions at the membrane surfaces. Periodic Bloch boundary conditions are used to connect the unit cells.

For the 5 μm period PnC, only frequencies up to 3 GHz were taken into account due to the limitations of the computation time. This computational heaviness was in large part caused by the large period, which in turn results in a comparatively small

Brillouin zone. The small Brillouin zone results in an increased number of foldings of the phonon branches at the edges of the first Brillouin zone. This then exponentially increases the computation time for the frequency eigenmodes.

Because of this omission of higher frequencies, the resulting emitted power data is only accurate at lower temperatures. As the temperature increases, higher frequencies are required for the dispersion data as more phonons are thermally exited. This gives rise to an approximately 50 % error at 400 mK for the 5 μm period data.

Figure 29 shows the simulated dispersion relations for an unaltered 300 nm SiN film, and for the same film with pillar-based PnC with a 5 μm period Al pillars. There appears to be no complete band gaps, but the bands are visibly flattened. For clarity, only a fraction of the calculated modes are shown in the plots. The dispersion relation for a 1 μm PnC is shown in Figure 30. Here the frequency range is larger, as the smaller period leads to a less heavy computation. Here a similar flattening is observed, and there even exists a complete band gap at around 2 GHz.

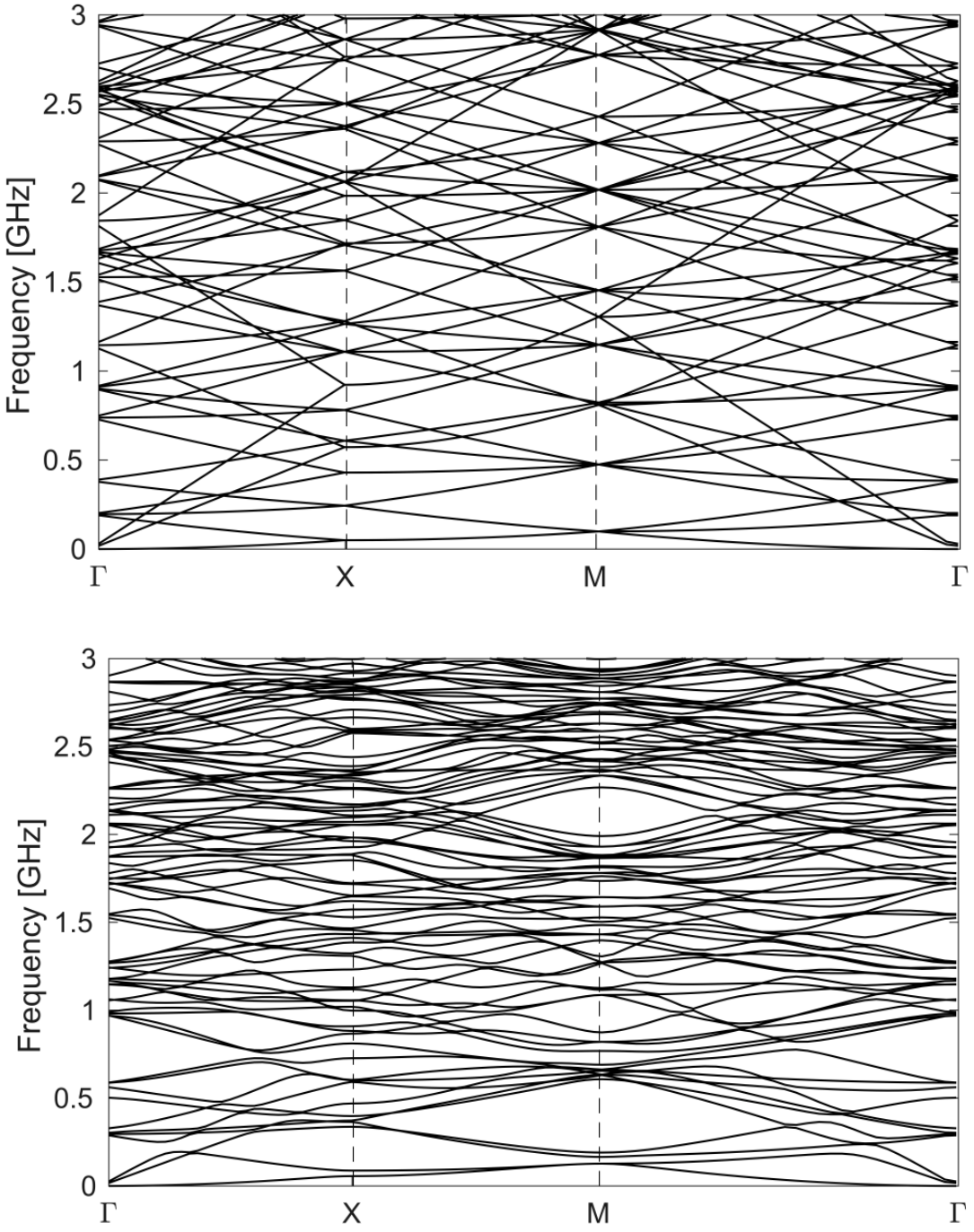

Figure 29. Simulated dispersion relations up to 3 GHz for an unaltered SiN film (upper) and a PnC with a 5 μm period Al pillar structure (lower).

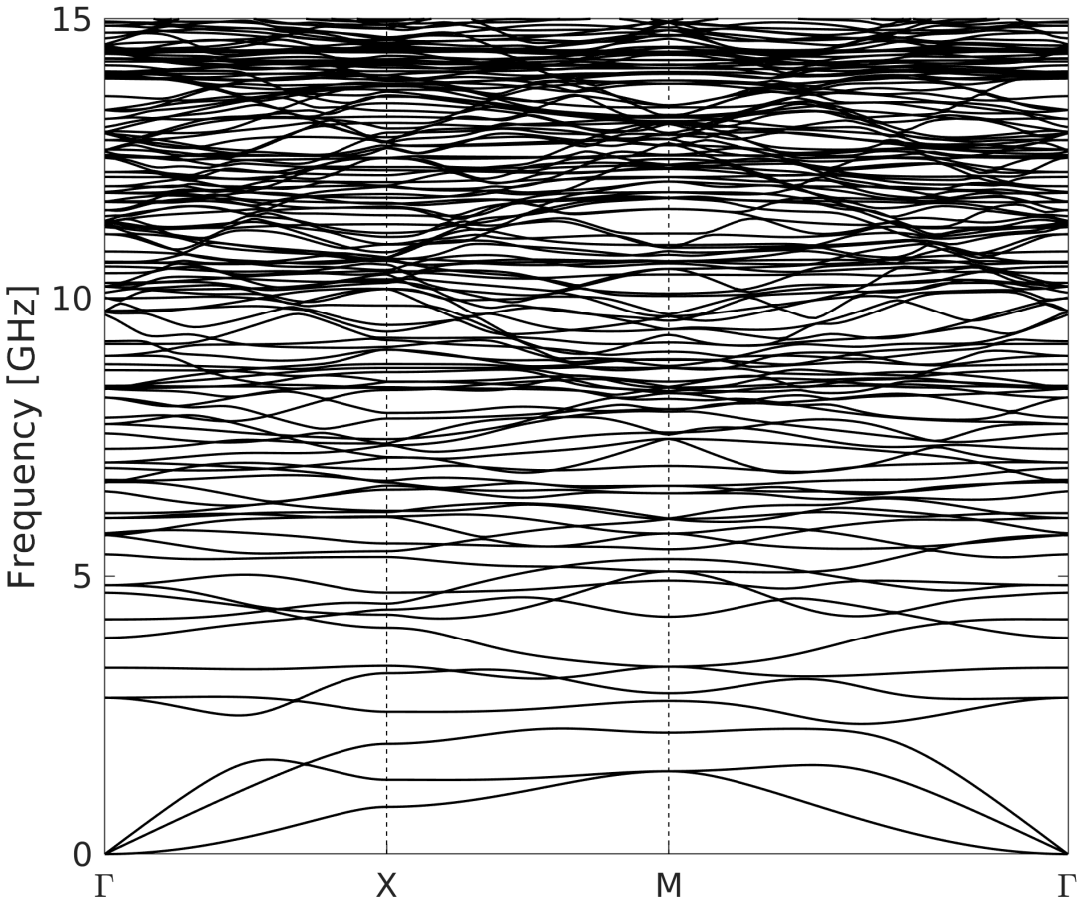

Figure 30. Dispersion relation for the 1 μm PnC.

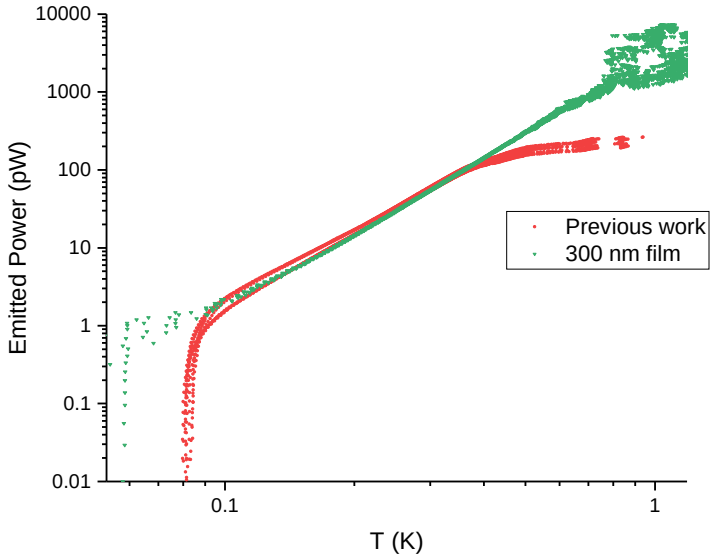

Figure 31. The unaltered membrane data compared with the previous results of Ref. [37]. The temperature exponent in the high temperature end for this particular previous work data set is 3.6.

5 Results and Discussion

5.1 Unaltered SiN film

The results for the emitted phonon power in a 300 nm SiN film (Figure 28) agreed well with previous results where a similar measurement geometry was used [37]. The film data and the data from Ref. [37] are plotted in Figure 31. The only difference between the data is a slightly higher power of 3.6-3.8 in the > 300 mK range in the previous measurement. The films in the two experiments were assumed to be of the same thickness, but as the chips were from a different wafer there may be differences in parameters such as stress.

In the SINIS IV- and differential conductance curves below 100 mK a peak near zero bias was observed, as can be seen in Figures 22 and 23. This peak was not observed in the previous experiments with the same heater-thermometer design [37].

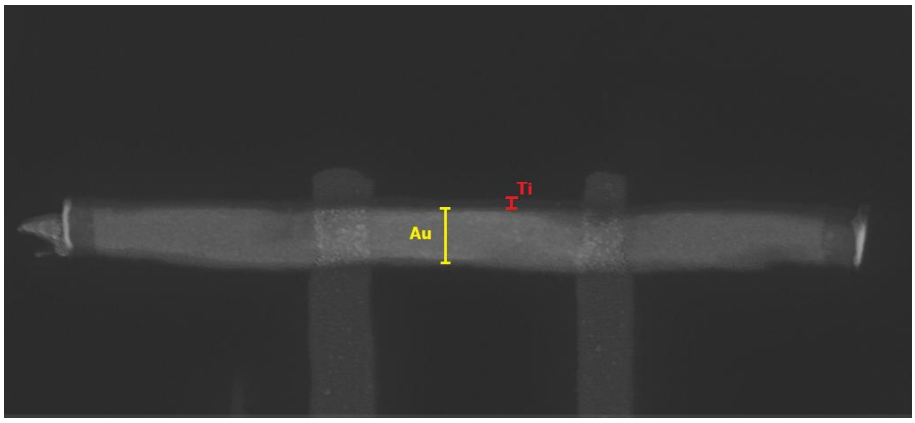

Figure 32. A close-up of a SINIS-junction where a possible Ti layer below the normal metal Au appears to extend around the Au, possibly shunting the normal metal.

A few possible explanations for this exist: Bulk titanium is a superconductor with a critical temperature of 0.49 K. It is plausible that the superconductivity of the Ti layer below the gold normal metal was not completely suppressed by the proximity effect [37]. This could result from the Ti layer being thicker than expected, resulting in a suppressed but finite T_c of $\sim$ 100 mK. In some SEM images (Figure 32) it was also observed that the area where Ti was deposited was larger than the area of Au, leaving a small part of the Ti exposed. This could also lead to the titanium shunting the normal metal. Both of these cases would result in a SIS′IS-junction, which would explain the zero bias current. The superconducting titanium being the source of the peak is also supported by the fact that no such peak can be seen in the IV-data from the measurement with the 5 µm or the 1 µm PnC sample, where the Ti layer thickness below the Au was reduced by 30 %.

A similar zero-bias peak below 100 mK in a differential conductance curve of a SINIS-junction has also been observed by for example Rajauria et al.. [82], where the conductance peak is explained to originate from Andreev current, a double particle tunnelling current induced by Andreev reflection. However, it is worthwhile to note that in [82] the normal metal used was copper. However, an Andreev current across a SINIS structure with a Ti-Au normal metal has been observed by Faivre et al. [83]. Instead of a current peak (Figure 23), the observed effect here was a step in the sub-gap current, so that does not fit to our results. Another fact discouraging the Andreev current as an explanation is that this peak has not been observed in any previous measurements with a similar junction performed in our research group.

Figure 28 includes the simulated curve for the emitted phonon power of the unaltered film. The agreement of the measured data and the theory is decent, but not perfect. The change of power law in the theory curve is different from the measured data. The power of the simulation curve in the same at the low temperature range, but at the high T range the power is 3.8. The power in the experimental data appears to be more closely aligned with the results of Ref. [37]. In Ref. [37] two different bias currents were used, one higher than the one used in this work. This provides a better sensitivity at higher temperatures, which could explain the difference at high temperatures.

There are a few factors which may explain the minor differences between the theory and the experiment. The elastic parameters for thin films are generally not well know, and even less so at low temperature. The simulations also assumed stress-free films (82), which is rarely the case in real thin films. The high temperature end of the measured data is also more prone to experimental error, as the sensitivity of the thermometer decreases in sensitivity above 500 K, as can be seen in Figure 27.

5.2 The emitted power of a 5 μm period phononic crystal

The IV-curves measured for an optimal bias current for the sample with the 5 μm aluminium pillar PnC with thermal model simulations are shown in Figure 33. Unfortunately, during the calibration and the heating experiment the cooling of the cryostat was not optimal, and the available calibration data extend only to around 100 mK, even though eventually a passable bath temperature of 85 mK was reached. This limits the measurement range at the lower temperatures.

Figure 34 presents the emitted power curve calculated from the heating experiment data with a power law fit. The exponent is very close to 4, and remains constant throughout the measurement range. This behaviour corresponds to the fully 3D case of equation (39). In the case of coherent phonon manipulation, as in Figure 4, the temperature exponent of the emitted power curve is expected to be lower than that of an unaltered film. In contrast to these results, the hole-based PnC curve also has a rather drastic change of power above 500 mK, perhaps caused by the coherence being destroyed at higher temperatures.

As for the 5 μm period Al pillar PnC, the most likely cause for the power of the

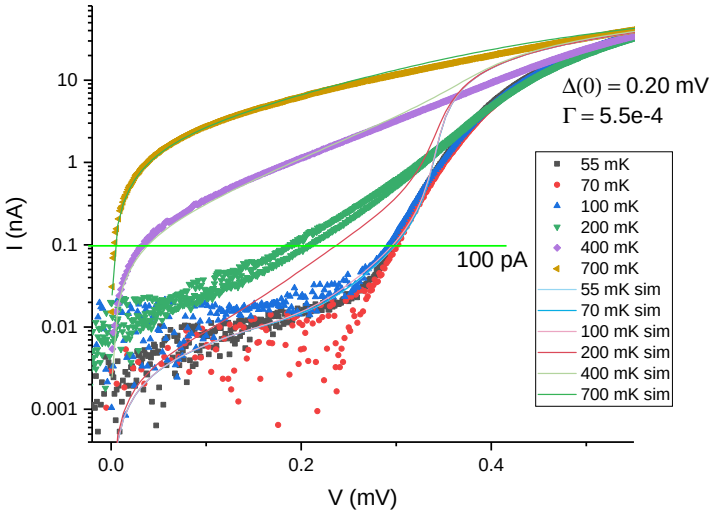

Figure 33. The IV-curves with thermal BCS-theory simulations for the SINIS-junction in the 5 µm PnC sample. The constant bias current used in the calibration and the heating experiment, which was identical to the one used in the unaltered film measurement, is also shown.

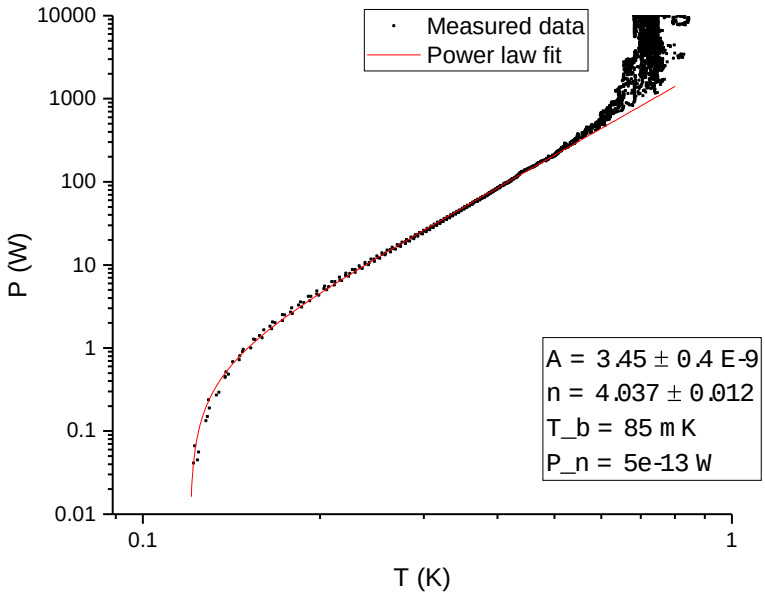

Figure 34. The emitted phonon power of the 5 µm period PnC with the power law fit.

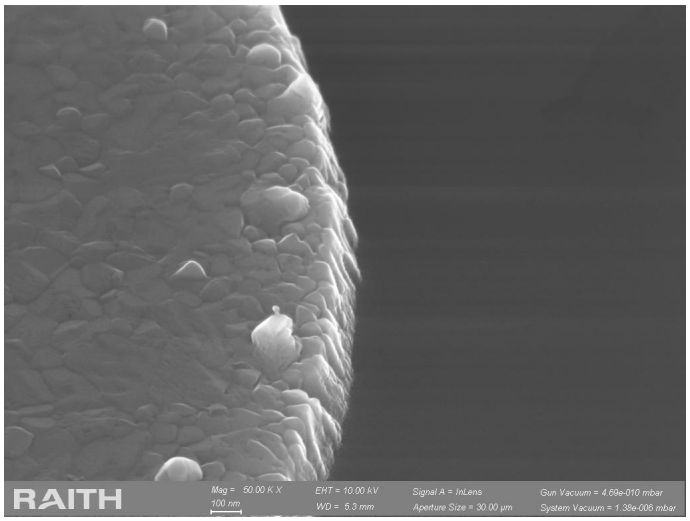

Figure 35. A high magnification SEM image of a single Al pillar. A notable surface roughness can be seen on the top of the pillar along with some large particles, and an even greater roughness is present on the sides of the pillar.

emitted power is the absence of coherent modification of the phonon disperions. If the phonons travelling in the film were incoherent and the phonon scattering would be diffusive, and the phonons would scatter to all possible directions within the film. Thus, equation (42) would no longer apply, and the situation would correspond to that of a 3D phonon gas encountering obstacles.

Figure 35 sheds light (or electrons) on what could destroy the coherence. Slight roughness is visible on the top of the pillars, and significantly more on the pillar sidewalls. In addition to that, there are some large particles up to 100 nm in diameter on the top of the pillar. From AFM images originally used for the calibration of the pillar height, the RMS surface roughness on the top of the pillars is ~ 3 nm. This also takes into account the large particles. The roughness on the sidewalls is much more difficult to quantitatively determine, but it appears to be around an order of magnitude greater that the top roughness. Based on equation (27) the roughness on the top of the pillars would still allow coherent effects, but the sidewall roughness would be enough to destroy the coherence. The quality of the interface between the aluminium and the SiN is also an unknown factor. If there is a significant mixture of the two materials at the interface, such as was shown in [65] for Al and Si, it could certainly affect the phonon scattering. It is also generally known that metal evaporation usually produces polycrystalline films. Based on Figure 35 this is also clearly the case here. These grain boundaries may also function as diffuse phonon

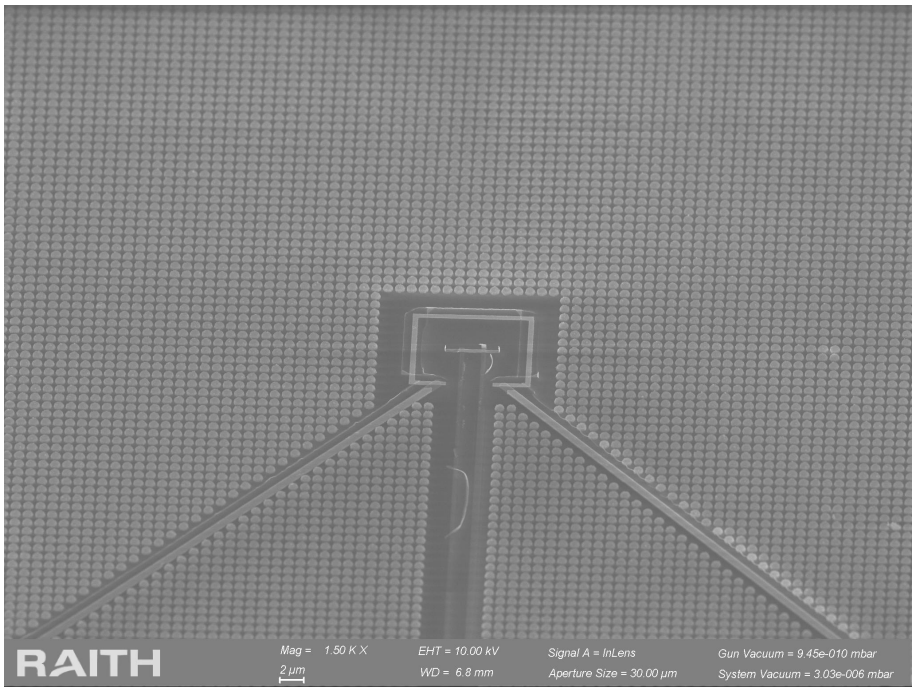

Figure 36. A SEM image of a sample with 1 µm period Al pillars.

scatterers.

5.3 The emitted power of a 1 µm period phononic crystal

The second phononic crystal sample measured was identical to the first sample, except it had a period of 1 µm (Figure 36). This time the cryostat worked better, and a bath temperature of 60 mK was reached, allowing for the investigation of the thermal conductance below 100 mK. The emitted power as a function of temperature for this sample along with the power law fit is presented in Figure 37. The behaviour here resembles the unaltered film more than the 5 µm sample, as there is again a visible change of the power law around 300 mK.

Unlike with the 5 µm PnC where the temperature dependence was $\sim T^4$, the temperature exponent is ~ 3 below 300 mK, lower than the unaltered film, and ~ 3.6 when $T > 300$ mK, which is higher than for the unaltered film. This dropping of the power below 4 can imply that the phonon propagation is no longer entirely incoherent, but coherent effects may start to emerge.

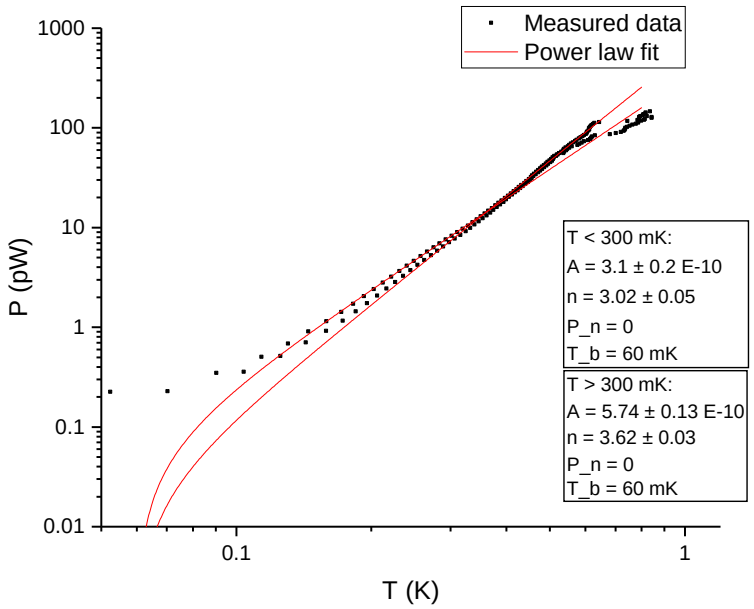

Figure 37. Emitted power for a 1 µm period PnC with a power law fit divided into two parts.

5.4 Discussion

The measured emitted power data of both the unaltered film and the 5 µm and the 1 µm PnCs along with the simulation data are plotted in Figure 38. As was discussed above, the 5 µm PnC simulation data extends only to 400 mK, and even at this temperature there exists a 50 % error. A notable reduction in thermal conductance is observed with the 5 µm PnC: around 66 % at 200 mK, 55 % at 300 mK, and getting smaller at higher temperatures. This appears to be even higher than the reduction predicted by the coherent theory in many previous numerical studies [25, 48, 53, 59], exluding ref. [61], where the reduction was much higher than what was obtained here. The reduction of the 1 µm PnC is even greater that with the 5 µm structure, approximately 85 % across the whole sensitivity range of the thermometer.

However, the simulations deliver a completely opposite behaviour. Here, the thermal conductance is predicted to decrease with a larger period, as is the case in other coherent theory studies [21, 24, 25]. This further reinforces our conclusion that the incoherent scattering is the dominant method of thermal conductance reduction for the 5 µm period structure.

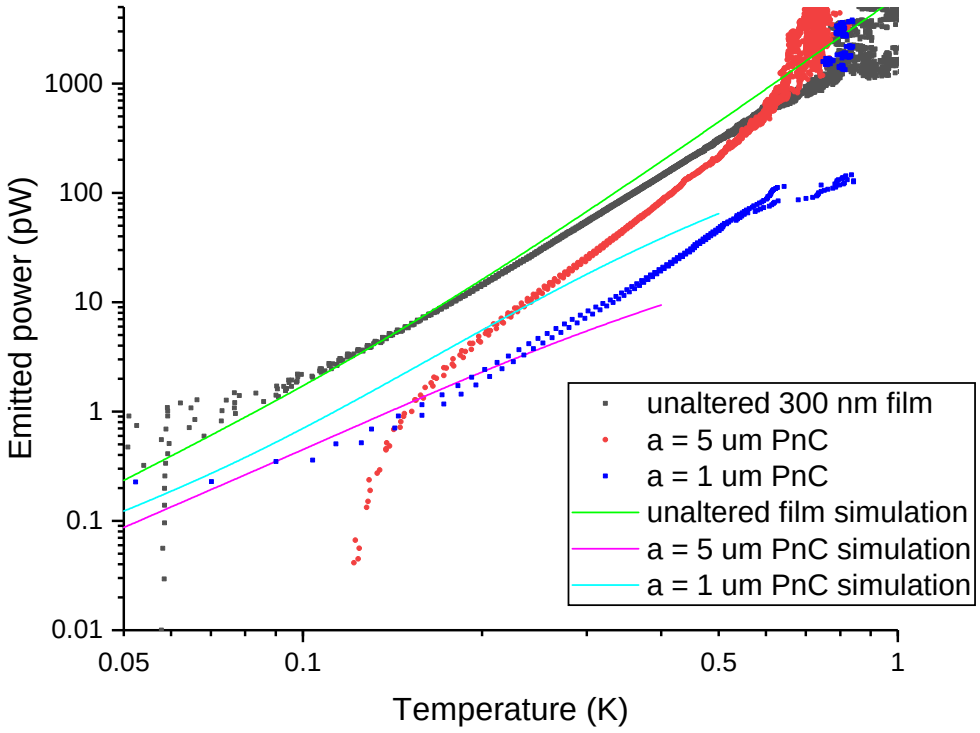

Figure 38. Numerical and experimental results for the emitted phonon power for the unaltered SiN film and the 5 μm and 1 μm period PnCs. Note the legends on the PnC theory curves, as the 5 μm simulation seems to correspond to the 1 μm experimental data, and vice versa.

If coherent thermal conductance reduction is suppressed or completely destroyed, the likely source for the observed reduction is phonons being backscattered from the pillars, which reduces the amount of phonons passing through the crystal. Local resonances could also play a role even in the incoherent case by preventing phonons with certain frequencies from propagating in the film. In a fully incoherent picture the difference between the 1 μm and the 5 μm sample can perhaps be explained by the results in [19] and [21], as the smaller period increases the scattering and reduces the phonon transmission probability. Nevertheless, as the 1 μm PnC does not appear fully incoherent based on the power of the T, some emerging coherent effects may also increase the reduction further.

In Ref. [67] the 7 to 10 μm period of the structures was relatively large, so it is reasonable to assume the origin of the reduction of the thermal conductance to be mostly incoherent. The larger reduction with the normal metal structures would also support this conclusion. As the reduction we observed is greater, and in Ref. [67] the smaller period produced a larger reduction, these results seem to agree with ours as a smaller period would produce a larger reduction in the incoherent case.

From the emitted phonon power data the thermal conductances were calculated with equation (46), where $\Delta T = T - T_b$. Figure 39 shows the thermal conductance for both the unaltered film and the PnCs. The unaltered film curve appears to turn upwards below 100 mK. This is most likely an artefact caused by the low sensitivity of the sensor at these temperatures, and also by the fact that the emitted power data appears to extend below the bath temperature.

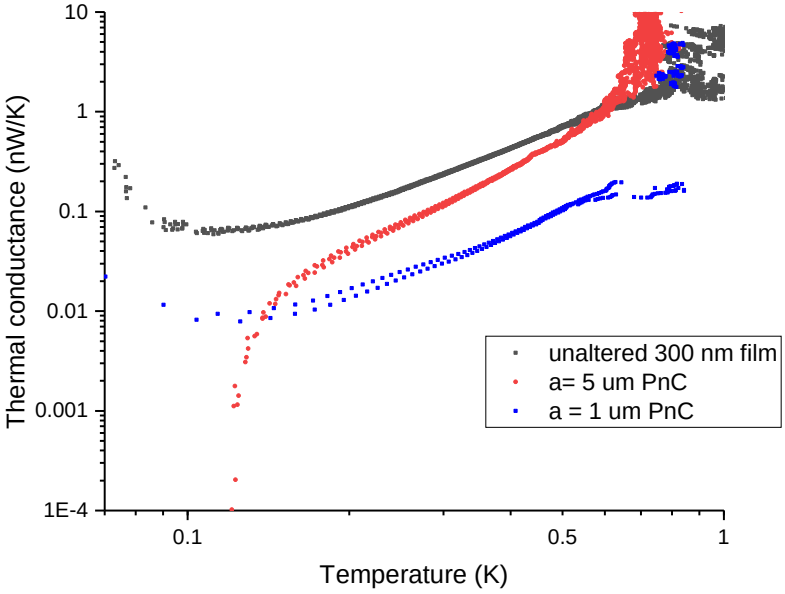

Figure 39. Thermal conductance of an unaltered SiN film and the PnCs with aluminium pillars with 5 μm and 1 μm periods calculated from the emitted power data.

6 Conclusions

In this thesis an aluminium pillar-based PnC was fabricated, and its thermal conductance was successfully measured in the temperature range of 60 mK - 1K. To our knowledge, the largest thermal conductance reduction via a pillar-based PnC was also observed. This shows that with some further development, the pillar-based PnCs could rival their hole-based counterparts in thermal conductance reduction, along with their other more favourable properties such as their higher durability and unchanged electrical conductance in semiconductor applications.

The observation of the reduction of the thermal conductance was an expected result, but the mechanism for this was tentatively concluded to be incoherent scattering instead of coherent phonon diffraction. As no incoherent simulations of the structure yet exist, it is left entirely to speculation whether there is any contribution for the thermal conductance reduction from the local resonances. When incoherent simulations are conducted, they could reveal if the incoherent scattering is the only remaining mechanism.

The most likely explanation for the absence of clearly coherent effects with the PnC is the roughness of the pillars. There are a number of approaches that could be taken to overcome this issue. As has been demonstrated in previous studies, the pillars could be directly etched from a single SiN film, which would give reduced roughness and also eliminate the interface between the pillars and the substrate. The pillars could also be etched from a metal film deposited on top of the film for a reduced roughness. An epitaxial deposition method could also be utilised to create atomically smooth surfaces.

The effects of different materials on the thermal conductance reduction, be it coherent or incoherent, should also be studied. As the thermal properties of a superconductor and a normal metal vary tremendously, comparison of the effects of normal and superconducting pillars to the thermal conductance could provide an interesting subject. Also, in contrast to a comparatively light element such as aluminium, a more dense material could be used to reach resonance frequencies at different frequency

range.

References

[1] M. Maldovan. "Narrow Low-Frequency Spectrum and Heat Management by Thermocrystals". In: *Phys. Rev. Lett.* 110.025902 (2 Jan. 2013). DOI: 10.1103/PhysRevLett.110.025902.

[2] M. S. Kushwaha et al. "Acoustic band structure of periodic elastic composites". In: *Physical Review Letters* 71 (13 Sept. 1993), pp. 2022–2025. DOI: 10.1103/PhysRevLett.71.2022.

[3] B. Goodwin, ed. *Photonic crystals : characteristics, performance and applications*. Physics research and technology. New York: Nova Science Publishers, Inc, 2017. URL: http://search.ebscohost.com/login.aspx?direct=true&scope=site&db=nlebk&AN=1453458.

[4] V. Laude. *Phononic Crystals : Artificial Crystals for Sonic, Acoustic, and Elastic Waves*. De Gruyter, Inc., 2015. URL: https://ebookcentral.proquest.com/lib/jyvaskyla-ebooks/detail.action?docID=4001494.

[5] M. Maldovan. "Sound and heat revolutions in phononics". In: *Nature* 502 (2013), pp. 209–217. DOI: 10.1038/nature12608.

[6] I. Maasilta et al. "Phononic Thermal Conduction Engineering for Bolometers: From Phononic Crystals to Radial Casimir Limit". In: *Journal of Low Temperature Physics* 184 (1 July 2016), pp. 211–216. DOI: 10.1007/s10909-015-1372-0.

[7] S. R. Sklan. "Splash, pop, sizzle: Information processing with phononic computing". In: *AIP Advances* 5.5 (2015), p. 053302. DOI: 10.1063/1.4919584.

[8] C. M. Reinke and I. El-Kady. "Phonon-based scalable platform for chip-scale quantum computing". In: *AIP Advances* 6.12 (2016), p. 122002. DOI: 10.1063/1.4972568.

[9] M. Pechal, P. Arrangoiz-Arriola, and A. H. Safavi-Naeini. “Superconducting circuit quantum computing with nanomechanical resonators as storage”. In: *Quantum Science and Technology* 4.1 (Sept. 2018), p. 015006. DOI: 10.1088/2058-9565/aadc6c.

[10] Y. Pennec et al. “Two-dimensional phononic crystals: Examples and applications”. In: *Surface Science Reports* 65.8 (2010), pp. 229–291. DOI: 10.1016/j.surfrep.2010.08.002.

[11] A. H. Aly, A. Mehaney, and M. F. Eissa. “Ionizing particle detection based on phononic crystals”. In: *Journal of Applied Physics* 118.6 (2015), p. 064502. DOI: 10.1063/1.4928315.

[12] M. Maldovan. “Phonon wave interference and thermal bandgap materials”. In: *Nature Materials* 14 (1 2015), pp. 667–674. DOI: https://doi.org/10.1038/nmat4308.

[13] J. Ravichandran et al. “Crossover from incoherent to coherent phonon scattering in epitaxial oxide superlattices”. In: *Nature Materials* 13 (Feb. 2014), pp. 168–172. DOI: 10.1038/nmat3826.

[14] R. Cheaito et al. “Interplay between total thickness and period thickness in the phonon thermal conductivity of superlattices from the nanoscale to the microscale: Coherent versus incoherent phonon transport”. In: *Physical Review B* 97.085306 (8 Feb. 2018). DOI: 10.1103/PhysRevB.97.085306.

[15] M. V. Simkin and G. D. Mahan. “Minimum Thermal Conductivity of Superlattices”. In: *Physical Review Letters* 84.927 (5 Jan. 2000). DOI: 10.1103/PhysRevLett.84.927.

[16] S.-M. Lee, D. G. Cahill, and R. Venkatasubramanian. “Thermal conductivity of SiGe superlattices”. In: *Applied Physics Letters* 70.22 (1997), pp. 2957–2959. DOI: 10.1063/1.118755.

[17] M. N. Luckyanova et al. “Coherent Phonon Heat Conduction in Superlattices”. In: *Science* 338.6109 (2012), pp. 936–939. DOI: 10.1126/science.1225549.

[18] N. Zen et al. “Engineering thermal conductance using a two-dimensional phononic crystal”. In: *Nature Communications* 5.3435 (2014). DOI: 10.1038/ncomms4435.

[19] J. Lee et al. “Investigation of phonon coherence and backscattering using silicon nanomeshes”. In: *Nature Communications* 8.14054 (Jan. 2017). DOI: 10.1038/ncomms14054.

[20] N. K. Ravichandran and A. J. Minnich. “Coherent and incoherent thermal transport in nanomeshes”. In: *Phys. Rev. B* 89.205432 (20 May 2014). DOI: 10.1103/PhysRevB.89.205432.

[21] Y. Tian et al. “Minimizing Coherent Thermal Conductance by Controlling the Periodicity of Two-Dimensional Phononic Crystals”. In: *Phys. Rev. Applied* 12 (1 July 2019), p. 014008. DOI: 10.1103/PhysRevApplied.12.014008.

[22] Z. Liu et al. “Locally Resonant Sonic Materials”. In: *Science* 289.5485 (2000), pp. 1734–1736. DOI: 10.1126/science.289.5485.1734.

[23] R. Anufriev and M. Nomura. “Phonon and heat transport control using pillar-based phononic crystals”. In: *Science and Technology of Advanced Materials* 19.1 (2018), pp. 863–870. DOI: 10.1080/14686996.2018.1542524.

[24] I. Maasilta and T. Puurtinen. “Low-Temperature Coherent Thermal Conduction in Thin Phononic Crystal Membranes”. In: *Crystals* 6.72 (2016). DOI: 10.3390/cryst6060072.

[25] R. Anufriev and M. Nomura. “Heat conduction engineering in pillar-based phononic crystals”. In: *Phys. Rev. B* 95 (15 Apr. 2017), p. 155432. DOI: 10.1103/PhysRevB.95.155432.

[26] B. L. Davis and M. I. Hussein. “Nanophononic Metamaterial: Thermal Conductivity Reduction by Local Resonance”. In: *Phys. Rev. Lett.* 112 (5 Feb. 2014), p. 055505. DOI: 10.1103/PhysRevLett.112.055505.

[27] J. M. Ziman. *Electrons and Phonons. The Theory of Transport Phenomena in Solids*. Great Clarendon Street, Oxford, Great Britain: Oxford University Press, 1960/2001. ISBN: 0198507798.

[28] N. W. Ashcroft and N. D. Mermin. *Solid State Physics*. Great Clarendon Street, Oxford, Great Britain: Thomson learning Inc., 1976. ISBN: 0030839939 (College Edition).

[29] C. Kittel. *Introduction to Solid State Physics*. 7th ed. Danvers: John Wiley & Sons, Inc., 1953/1996.

[30] A. N. Cleland. *Foundations of Nanomechanics. From Solid-State Theory to Device Applications*. Springer, 2003. ISBN: 9783662052877.

[31] T. A. Puurtinen and I. J. Maasilta. "Low temperature heat capacity of phononic crystal membranes". In: *AIP Advances* 6.12 (2016), p. 121902. DOI: 10.1063/1.4968619.

[32] J. Galsin. *Solid State Physics: An Introduction to Theory*. Elsevier Science, 2019. ISBN: 9780128171042.

[33] H. F. C. Hoevers et al. "Radiative ballistic phonon transport in silicon-nitride membranes at low temperatures". In: *Applied Physics Letters* 86.25 (2005), p. 251903. DOI: 10.1063/1.1949269.

[34] A. A. Maznev. "Boundary scattering of phonons: Specularity of a randomly rough surface in the small-perturbation limit". In: *Phys. Rev. B* 91 (13 Apr. 2015), p. 134306. DOI: 10.1103/PhysRevB.91.134306.

[35] T. Korkiamäki. "Optimisation of the etching profile of silicon nitride in reactive ion etching". Research training report. University of Jyväskylä, Department of physics, 2019.

[36] K. F. Graff. *Wave motion in elastic solids*. London, UK: Oxford University Press, 1975/1991. URL: https://archive.org/details/wavemotioninelas00graf/mode/2up.

[37] T. Loippo. "2D phonon thermal transport in thin SiN film". Master's thesis. University of Jyväskylä, Department of physics, 2019.

[38] T. Kühn and I. J. Maasilta. "Maximizing phonon thermal conductance for ballistic membranes". In: *Journal of Physics: Conference Series* 92 (Dec. 2007), p. 012082. DOI: 10.1088/1742-6596/92/1/012082.

[39] T. Kühn and I. Maasilta. "Ballistic phonon transport in dielectric membranes". In: *Nuclear Instruments and Methods in Physics Research Section A: Accelerators, Spectrometers, Detectors and Associated Equipment* 559.2 (2006), pp. 724–726. ISSN: 0168-9002. DOI: https://doi.org/10.1016/j.nima.2005.12.118.

[40] R. Anufriev, J. Maire, and M. Nomura. "Reduction of thermal conductivity by surface scattering of phonons in periodic silicon nanostructures". In: *Physical Review B* 93 (Jan. 2016). DOI: 10.1103/PhysRevB.93.045411.

[41] G. Xie et al. “Ultra-low thermal conductivity of two-dimensional phononic crystals in the incoherent regime”. In: *npj Computational Materials* 4.20 (2018). DOI: 10.1038/s41524-018-0076-9.

[42] C. Jeong, S. Datta, and M. Lundstrom. “Full dispersion versus Debye model evaluation of lattice thermal conductivity with a Landauer approach”. In: *Journal of Applied Physics* 109.7 (2011), p. 073718. DOI: 10.1063/1.3567111.

[43] R. Anufriev and M. Nomura. “Thermal conductance boost in phononic crystal nanostructures”. In: *Phys. Rev. B* 91 (24 June 2015), p. 245417. DOI: 10.1103/PhysRevB.91.245417.

[44] P. E. Hopkins et al. “Reduction in the Thermal Conductivity of Single Crystalline Silicon by Phononic Crystal Patterning”. In: *Nano Letters* 11.1 (2011), pp. 107–112. DOI: 10.1021/nl102918q.

[45] R. Anufriev and M. Nomura. “Reduction of thermal conductance by coherent phonon scattering in two-dimensional phononic crystals of different lattice types”. In: *Phys. Rev. B* 93 (4 Jan. 2016), p. 045410. DOI: 10.1103/PhysRevB.93.045410. URL: https://link.aps.org/doi/10.1103/PhysRevB.93.045410.

[46] M. Hirsekorn. “Small-size sonic crystals with strong attenuation bands in the audible frequency range”. In: *Applied Physics Letters* 84.17 (2004), pp. 3364–3366. DOI: 10.1063/1.1723688.

[47] A. Khelif, Y. Achaoui, and B. Aoubiza. “In-plane confinement and waveguiding of surface acoustic waves through line defects in pillars-based phononic crystal”. In: *AIP Advances* 1.4 (2011), p. 041404. DOI: 10.1063/1.3675923.

[48] A. Khelif, Y. Achaoui, and B. Aoubiza. “Surface acoustic waves in pillars-based two-dimensional phononic structures with different lattice symmetries”. In: *Journal of Applied Physics* 112.3 (2012), p. 033511. DOI: 10.1063/1.4737780.

[49] A. Khelif et al. “Locally resonant surface acoustic wave band gaps in a two-dimensional phononic crystal of pillars on a surface”. In: *Phys. Rev. B* 81 (21 June 2010), p. 214303. DOI: 10.1103/PhysRevB.81.214303.

[50] R. Pourabolghasem et al. “Physics of band-gap formation and its evolution in the pillar-based phononic crystal structures”. In: *Journal of Applied Physics* 116.1 (2014), p. 013514. DOI: 10.1063/1.4887115.

[51] B. Graczykowski et al. “Phonon dispersion in hypersonic two-dimensional phononic crystal membranes”. In: *Phys. Rev. B* 91 (7 Feb. 2015), p. 075414. DOI: 10.1103/PhysRevB.91.075414.

[52] J.-C. Hsu. “Local resonances-induced low-frequency band gaps in two-dimensional phononic crystal slabs with periodic stepped resonators”. In: *Journal of Physics D: Applied Physics* 44.5 (Jan. 2011), p. 055401. DOI: 10.1088/0022-3727/44/5/055401.

[53] Y. Achaoui et al. “Local resonances in phononic crystals and in random arrangements of pillars on a surface”. In: *Journal of Applied Physics* 114.10 (2013), p. 104503. DOI: 10.1063/1.4820928.

[54] Y. Achaoui et al. “Experimental observation of locally-resonant and Bragg band gaps for surface guided waves in a phononic crystal of pillars”. In: *Phys. Rev. B* 83 (10 Mar. 2011), p. 104201. DOI: 10.1103/PhysRevB.83.104201.

[55] M. G. Holland. “Analysis of Lattice Thermal Conductivity”. In: *Physical Review* 132.2461 (1963). DOI: 10.1103/PhysRev.132.2461.

[56] H. Honarvar and M. I. Hussein. “Spectral energy analysis of locally resonant nanophononic metamaterials by molecular simulations”. In: *Phys. Rev. B* 93 (8 Feb. 2016), p. 081412. DOI: 10.1103/PhysRevB.93.081412.

[57] H. Honarvar, L. Yang, and M. I. Hussein. “Thermal transport size effects in silicon membranes featuring nanopillars as local resonators”. In: *Applied Physics Letters* 108.26 (2016), p. 263101. DOI: 10.1063/1.4954739.

[58] Z. Wei et al. “Phonon transport properties in pillared silicon film”. In: *Journal of Applied Physics* 118.15 (2015), p. 155103. DOI: 10.1063/1.4933284.

[59] S. Xiong et al. “Blocking Phonon Transport by Structural Resonances in Alloy-Based Nanophononic Metamaterials Leads to Ultralow Thermal Conductivity”. In: *Phys. Rev. Lett.* 117 (2 July 2016), p. 025503. DOI: 10.1103/PhysRevLett.117.025503.

[60] R. Anufriev and M. Nomura. “Coherent Thermal Conduction in Silicon Nanowires with Periodic Wings”. In: *Nanomaterials* 9.142 (2 2019). DOI: 10.3390/nano9020142.

[61] H. Honarvar and M. I. Hussein. "Two orders of magnitude reduction in silicon membrane thermal conductivity by resonance hybridizations". In: *Phys. Rev. B* 97 (19 May 2018), p. 195413. DOI: 10.1103/PhysRevB.97.195413.

[62] M. Sledzinska et al. "Fabrication of phononic crystals on free-standing silicon membranes". In: *Microelectronic Engineering* 149 (2016), pp. 41–45. ISSN: 0167-9317. DOI: https://doi.org/10.1016/j.mee.2015.09.004.

[63] D. Yudistira et al. "Nanoscale pillar hypersonic surface phononic crystals". In: *Phys. Rev. B* 94 (9 Sept. 2016), p. 094304. DOI: 10.1103/PhysRevB.94.094304.

[64] A. Iskandar et al. "Modification of the phonon spectrum of bulk Si through surface nanostructuring". In: *Journal of Applied Physics* 120.9 (2016), p. 095106. DOI: 10.1063/1.4962208.

[65] R. Anufriev, R. Yanagisawa, and M. Nomura. "Aluminium nanopillars reduce thermal conductivity of silicon nanobeams". In: *Nanoscale* 9 (39 2017), pp. 15083–15088. DOI: 10.1039/C7NR05114J.

[66] X. Huang et al. "Thermal Conductivity Reduction in a Silicon Thin Film with Nanocones". In: *ACS Applied Materials & Interfaces* 11 (Sept. 2019). DOI: 10.1021/acsami.9b08797.

[67] X. Zhang et al. "Controlling the thermal conductance of silicon nitride membranes at 100 mK temperatures with patterned metal features". In: *Applied Physics Letters* 115.5 (2019), p. 052601. DOI: 10.1063/1.5097173.

[68] F. Giazotto et al. "Opportunities for mesoscopics in thermometry and refrigeration: Physics and applications". In: *Rev. Mod. Phys.* 78 (1 Mar. 2006). DOI: 10.1103/RevModPhys.78.217.

[69] P. Koppinen, T. Kühn, and I. Maasilta. "Effects of Charging Energy on SINIS Tunnel Junction Thermometry". In: *Journal of Low Temperature Physics* 154.5-6 (2009), pp. 179–189. DOI: 10.1007/s10909-009-9861-7.

[70] M. R. Nevala et al. "Sub-micron normal-metal/insulator/superconductor tunnel junction thermometer and cooler using Nb". In: *Applied Physics Letters* 101.11 (2012), p. 112601. DOI: 10.1063/1.4751355.

[71] S. Chaudhuri, M. R. Nevala, and I. J. Maasilta. "Niobium nitride-based normal metal-insulator-superconductor tunnel junction microthermometer". In: *Applied Physics Letters* 102.13 (2013), p. 132601. DOI: 10.1063/1.4800440.

[72] J. Bardeen, L. N. Cooper, and J. R. Schrieffer. "Theory of Superconductivity". In: *Phys. Rev.* 108 (5 Dec. 1957). DOI: 10.1103/PhysRev.108.1175.

[73] M. Tinkham. *Introduction to Superconductivity*. 2nd ed. McGraw-Hill Inc., 1973/1996. ISBN: 0070648786.

[74] T. T. Heikkiä. *The Physics of Nanoelectronics. Transport and Fluctuation Phenomena at Low temperatures*. Oxford, UK: Oxford University Press, 2013. ISBN: 9780199592449.

[75] G. E. Blonder, M. Tinkham, and T. M. Klapwijk. "Transition from metallic to tunneling regimes in superconducting microconstrictions: Excess current, charge imbalance, and supercurrent conversion". In: *Phys. Rev. B* 25 (7 Apr. 1982), pp. 4515–4532. DOI: 10.1103/PhysRevB.25.4515.

[76] C. B. Satterthwaite. "Thermal Conductivity of Normal and Superconducting Aluminum". In: *Phys. Rev.* 125 (3 Feb. 1962), pp. 873–876. DOI: 10.1103/PhysRev.125.873.

[77] J. Bardeen, G. Rickayzen, and L. Tewordt. "Theory of the Thermal Conductivity of Superconductors". In: *Phys. Rev.* 113 (4 Feb. 1959), pp. 982–994. DOI: 10.1103/PhysRev.113.982.

[78] I. M. W. Räisänen et al. "Normal metal - insulator - superconductor thermometers and coolers with titanium-gold bilayer as the normal metal". In: *Journal of Physics: Conference Series* 969 (Mar. 2018), p. 012090. DOI: 10.1088/1742-6596/969/1/012090.

[79] K. E. Bean. "Anisotropic etching of silicon". In: *IEEE Transactions on Electron Devices* 25.10 (Oct. 1978), pp. 1185–1193. ISSN: 1557-9646. DOI: 10.1109/T-ED.1978.19250.

[80] M. Nevala. "Development of niobium-based superconducting junctions". PhD thesis. University of Jyväskylä, Department of physics, Aug. 2012.

[81] M. D. Henry et al. "Degradation of Superconducting Nb/NbN Films by Atmospheric Oxidation". In: *IEEE Transactions on Applied Superconductivity* 27.4 (June 2017). ISSN: 2378-7074. DOI: 10.1109/TASC.2017.2669583.

[82] S. Rajauria et al. "Andreev Current-Induced Dissipation in a Hybrid Superconducting Tunnel Junction". In: *Phys. Rev. Lett.* 100 (20 May 2008), p. 207002. DOI: 10.1103/PhysRevLett.100.207002.

[83] T. Faivre, D. S. Golubev, and J. P. Pekola. “Andreev current for low temperature thermometry”. In: *Applied Physics Letters* 106.18 (2015), p. 182602. DOI: 10.1063/1.4919892.